1-1-2014

Rydberg Time-Of-Flight And Imaging Probes Of The Velocity-Dependent Hydrogen Atom Spin Polarization

Bernadette Michlewicz Broderick
Wayne State University,

RYDBERG TIME-OF-FLIGHT AND IMAGING PROBES OF THE VELOCITY-DEPENDENT HYDROGEN ATOM SPIN POLARIZATION

by

BERNADETTE MICHLEWICZ BRODERICK

DISSERTATION

Submitted to the Graduate School

of Wayne State University,

Detroit, Michigan

in partial fulfillment of the requirements

for the degree of

DOCTOR OF PHILOSOPHY

2014

MAJOR: CHEMISTRY

Approved By:

_____

Advisor Date

_____

_____

_____

DEDICATION

To my family.

In loving memory of Denise Michlewicz Broderick.

ACKNOWLEDGEMENTS

It is an impossible task to adequately convey the gratitude I feel to those people mentioned below. From the very bottom of my heart, I thank you all.

First and foremost, I thank my PhD advisor, Arthur Suits. Working for you was a transformative experience. Thank you for giving me an exhilarating experiment – we cast the doors wide open! But most importantly, thank you for your kindness. I entered your laboratory as a naive rube, and even with your massive operation full of exciting experiments, you always made time to teach me. I owe who I am as a scientist to you. To have been witness to your creative wizardry and explosive enthusiasm is a gift I will treasure forever. Thank you for believing in me.

I thank the staff members at Wayne State, especially Melissa Barton; I would not have graduated had it not been for your administrative miracles after my numerous delinquent registrations. To Diane Kudla, Bernie Milesk, and Debbie McCreless, for their patience with my inherent inability to file important papers in a timely fashion, and never complaining about it.

Thank you Jimmy England, who has been with me since we were confused under- graduate scientists, and whose sense of humor was always accessible, and never disappointing.

Thank you Yumin Lee, whose frustration threshold vastly exceeded mine, and without which we would have been witness to fewer interesting observations. It was my pleasure to have ventured into the unknown SPH territory with you, and to have come out alive, having learned something new.

Thank you Ravin F. Lakshitha, for teaching me to forever dwell in the land of the positive. I will always cherish our offensive exchanges.

Thank you James Oldham and Kirill Prozument, who regularly exuded their post- doc-ish confidence that there are always rational explanations for what we observed (or didn't observe) in the lab.

Thank you Vladimir Chernyak; for your patience as it relates to my mathematical ineptitude, and for your devotion to this project which resulted in a number of fresh perspectives that helped propel SPH to new heights. Thank you for teaching me spectroscopy, Russian optimism, and tennis; and for being a friend.

Thank you Fadia Cudry, who has been by my side from the very beginning. You gave so much to me these last 5 years. A shoulder to cry on, a sense of humor, a niece, and an inseparable bond. Thank you for your love and loyalty.

I thank the National Science Foundation for funding this project, award number 1111348.

Most importantly, I thank my family. To my parents, who sacrificed everything for their five children. Thank you dad for teaching me to be tough, and inspired, and passionate, in all of life's arenas. I would be lost without your unconditional love and support. I thank my mom, who always told me to think, and whose quick wit and quirky spirit made difficult times tolerable. Your strength was as critical as it were immeasurable. Thank

you Stefanie, for rescuing me on countless hopeless occasions. You have been a sister, a mother, and a loyal ally to me since we were kids with nylons on our heads. Thank you John, for your tireless competitive spirit that has always kept me on my toes, and for your quiet generosity towards our family. Thank you Joe, for the kindness you have so freely given to me. You have been an extraordinarily reliable source of fun and compassion in my life. Thank you Hannah, for being my loyal bunk mate, and dear friend. Your fierce pursuit of the unconventional has been inspirational, and your unwavering support for me has been invaluable. Thank you Norm, for enriching my life in an infinite number of dimensions.

This work would have remained but a dream without the love and support of my family. I dedicate this thesis to them.

TABLE OF CONTENTS

LIST OF FIGURES

INTRODUCTION

1.1 Dynamical Stereochemistry

Chemical reactions are intrinsically anisotropic. Upon collision with a photon, surface, or atom, a molecule will always prefer certain angles of approach and separation, as well as certain planes of rotation [13]. Early experiments seeking to understand the nature of these collision dynamics were largely confined to the measurement of scalar properties, such as the energy partitioning into translation and other various degrees of freedom [14] [15] [16]. Today, these scalar properties have been augmented by a powerful new class of experiments focused on "vector correlations" [17], [18]. Here, the velocity and angular momentum vectors and their correlations are measured for atoms or molecules often with single quantum state specificity, revealing both magnitude and direction-dependent information. These are the key indicators of these anisotopic forces which govern dynamical phenomena. Through conservation of energy and momentum laws, scalar and vector properties can then be correlated with each other, as well as the unmeasured cofragment, and subsequently used to elucidate the very nature of the entire collision event [19], [20], [21].

This ability to interrogate the role of spatial anisotropy directly has enriched the field of chemical reaction dynamics. Photodissociation experiments, in which reactive processes can be studied under well-controlled conditions, are an ideal environment in which to apply these vector correlation methods. Here, deep

insight into the underlying features of the photoexcitation process, as well as the subsequent dissociation dynamics across multiple electronic states can be achieved [19], [20], [21]. Vector correlations have led to observation of a series of remarkable new phenomena, such as the observation of a pure coherent quantum mechanical mechanism for production of atomic photofragment polarization [4] [22], observation of coherences showing that the electron cloud in the recoiling atom "remembers" the original molecular plane [23] [24], and observation of the energy-dependent quantum oscillations in the cross section of photofragment polarization [25], [26], [27]. These oscillations are a manifestation of the "matter-wave" interference along multiple dissociative continua, a quantum effect revealed experimentally by these state-specific vector correlation methods.

Vector correlation studies in photodissociation were originally directed to probing rotational angular momemtum polarization [28] [29]. With the advent of imaging methods, atomic orbital polarization became a natural target for these studies. A variety of atomic species in photodissociation and collision experiments have been studied with the vector correlation approach, including Cl [30], [31], Br [32], [33], [30], S [34], [32], [33], and O [35], [36]. A prime candidate for which to apply these methods is the hydrogen atom, a ubiquitous photoproduct and the most abundant atom in the universe. However, the only form of angular momentum is spin, and for several reasons, it has not been possible to measure this directly in a photodissociation experiment. Briefly, this includes the need to resolve the fine structure, while at the same time measuring its recoil velocity which typically has a Doppler width many times larger than the largest fine structure splitting.

This dissertation reports a new experimental approach which generalizes these powerful vector correlation methods through application to the H atom. Here, measurement of the velocity-dependent H atom spin-polarization is demonstrated experimentally for the very first time [37]. The technique, termed $Spin-Polarized\ Hydrogen\ Rydberg\ Time-of-Flight$, more than doubles the number of observables accessible in these experiments: at each recoil speed we determine the number of H atoms scattered at that speed, as well as the incoherent and coherent contributions to the spin polarization produced in photodissociation [38]. As these studies make use of polarized light to initiate dissociation, the H atom spin can be utilized as a reporter on orbital orientation [23], [39], nonadiabatic dynamics [30], and coherent dissociation mechanisms underlying these processes [40], [27].

Vector correlations are characterized by the moments of the magnetic sublevel distribution: the population, which is independent of the magnetic sublevel distribution m_j distribution, the orientation, which is proportional to the dipole moment of the ensemble and implies a nonstatistical m_j distribution, or the alignment, which is proportional to the quadrupole moment of the ensemble and implies a nonstatistical $|m_j|$ distribution [41]. A general overview of the vector correlations considered in this work is as follows: 1) μ, the transition dipole moment of the parent molecule; 2) $\mathbf{E}$, the polarization of the dissociation light; 3) $\mathbf{v}$, the photofragment recoil velocity; and 4) s, spin, which is the only form of angular momentum in the ground state H atom.

1.1.1 E-μ-v Correlation: Recoil Velocity Anisotropy

The E-μ-v correlation reflects the overall angular distribution of the photofragments, β, with respect to the parent molecule's transition dipole moment, μ. It is the most widely reported vector correlation in photodissociation experiments [42].

The angular distribution I(θ) about the polarization of the photolysis laser beam is given by the following equation:

$$\mathrm{I}(\theta) \propto 1 + \beta(P_2(\cos\theta)) \tag{1.1}$$

θ represents the angle between the recoil direction and the polarization of the photolysis light, and P_2 is the second-order Legendre polynomial. This relationship arises as a consequence of the fact that the absorption probability is proportional to E $\cdot$ μ^2 [18]. Thus, immediately following absorption, the parent molecules are aligned such that the probability of finding the angle, θ, between μ and the electric field vector E varies as $\cos^2$ [43].

To a first approximation, the magnitude and sign of β are determined purely by the symmetry of the state that is accessed when the parent molecule absorbs the dissociating light [39]. β has limiting values of -1 to + 2, which correspond to purely perpendicular and purely parallel events, respectively. Figure 1.1 below represents both of these limiting cases within the axial recoil approximation.

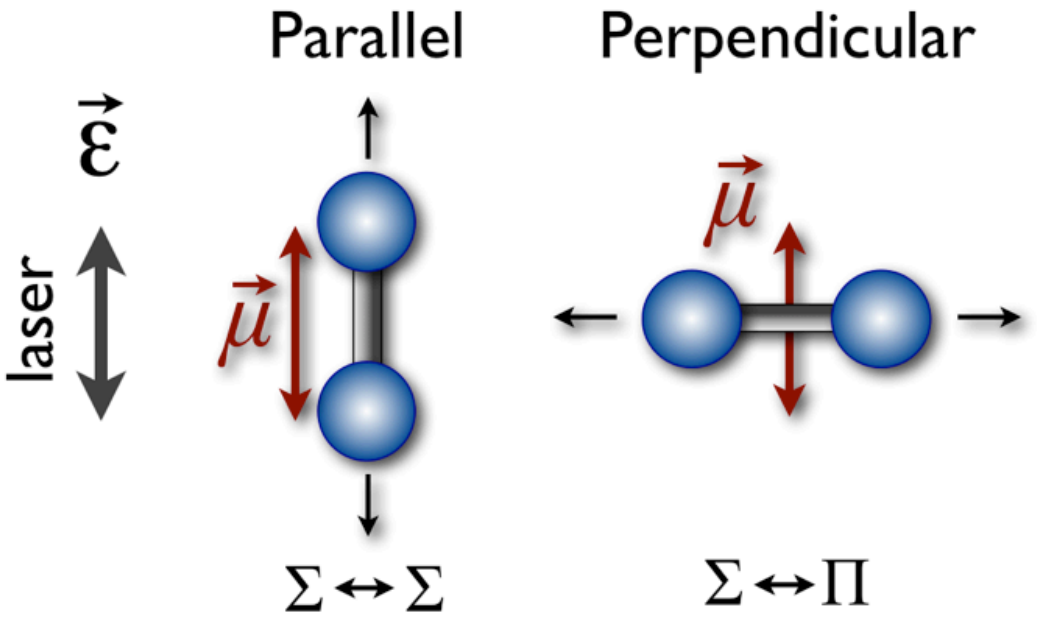

FIGURE 1.1: Limiting values of the overall angular distribution for diatomic systems where Ω is a good quantum number.

Intermediate values are associated with mixed transitions of both perpendicular and parallel character. While β yields insight into the nature of the electronic transition of the parent molecule and the relative symmetry of the transition, over the course of dissociation the spatial anisotropy can be substantially modified [39]; thus, β does not tell the whole story. The angular distribution alone does not reveal details of the nonadiabatic dynamics, long-range interactions, and coherent effects in dissociation. However, it is possible to obtain a complete description of the individual photofragment angular momentum distributions, which afford additional insight into the photodissociation process. These are discussed below.

1.1.2 E-μ-J Correlation: Angular Momentum Polarization

Early studies of the angular momentum polarization in atoms and molecules were largely focused on the correlation between the translation and rotational motion

of a molecular photofragment. Dixon et al defined this correlation with a semiclassical approach wherein a series of bipolar harmonics were used to describe the translation and rotational angular distributions, and subsequently used to elucidate the dynamics of a photodissociation event [44]. Semiclassical models adequately describe the high-**J** rotational polarization, but fail at low-**J** rotational values. Alternatives to this semiclassical treatment include the Hall density matrix approach [18], and a fully quantum mechanical treatment by Siebbeles et al. wherein the recoil angle dependence of angular momentum polarization is expressed in terms of scattering matrix elements [45] . The E-μ-J correlation described here is expressed in terms of the multipole moments $p_K Q$ given by Seibbeles, where K and Q represent the system rank and component, respectively. The zeroth order multipole moment corresponds to the population, while the higher-order odd moments describe the *orientation*, and the even moments describe the *alignment* [41]. Any orientation or alignment observed experimentally implies a nonequilibrium population of the magnetic sublevels m_J, which are the projection of the *total* angular momentum **J** onto the recoil axis. Orientation represents a *unidirectional* distribution of **J**, whereas alignment represents a *bidirectional* distribution of **J**. Moreover, orientation corresponds to unequal populations changing with m_J, whereas alignment corresponds to population changes in $|m_J|$ [41]. Figure 1.2 summarizes these different distributions [42], and a thorough discussion of the state multipole treatment is provided in Chapter 3 here. It should be noted that the H atom is a rank K = 1 system, and thus the only multipole moments relevant to these studies are the population and orientation distributions. Alignment is only possible in K = 2 or higher-order systems.

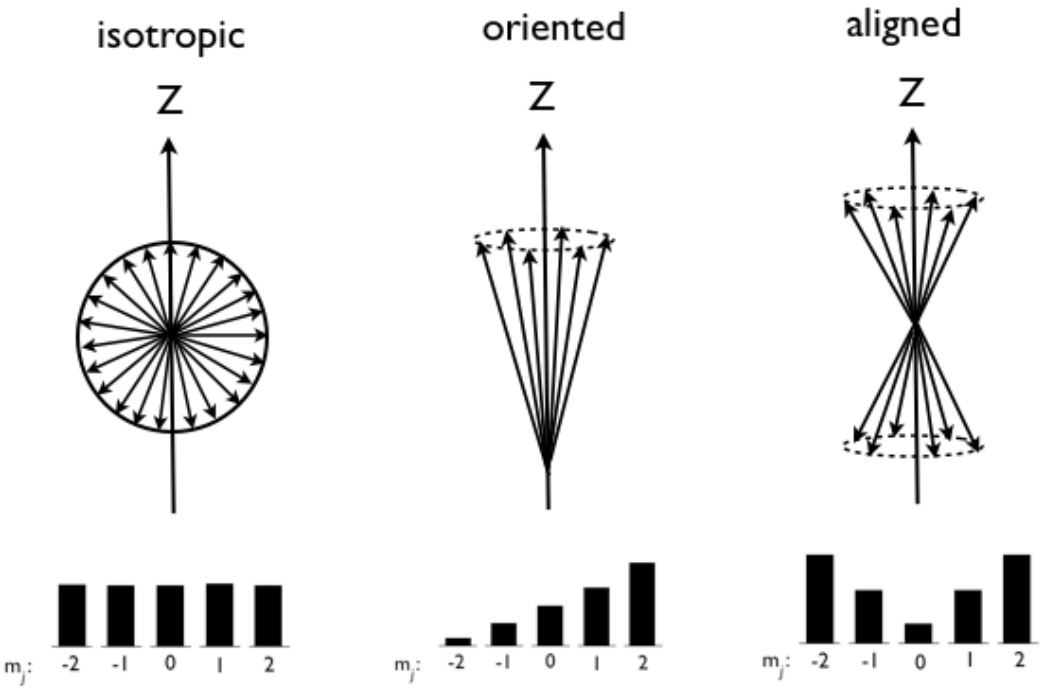

FIGURE 1.2: Isotropic, oriented, and aligned distributions with corresponding magnetic sublevel populations.

1.1.3 v-J Correlation

In contrast to the overall spatial anisotropy of a molecule, measurement of the *electronic* angular momentum of atomic photofragments can provide deep insight into fundamental dynamical processes; here, the electronic structure over the course of dissociation is exclusively responsible for the experimentally observed orientation. Features of the electronic landscape which are intrinsically difficult to navigate theoretically, but yield experimentally observable orientation include the symmetry of the excited electronic state, coherent excitation of multiple electronic states, Coulomb interation at large internuclear separation, nonadiabatic transitions at avoided crossings, and nonadiabatic transitions at large internuclear separations (see Figure 1.3). The resulting preferred direction of **J** and its correlation with **v** thus becomes a powerful tool for disentangling these nonadiabatic phenoma and their contribution to dissociation dynamics.

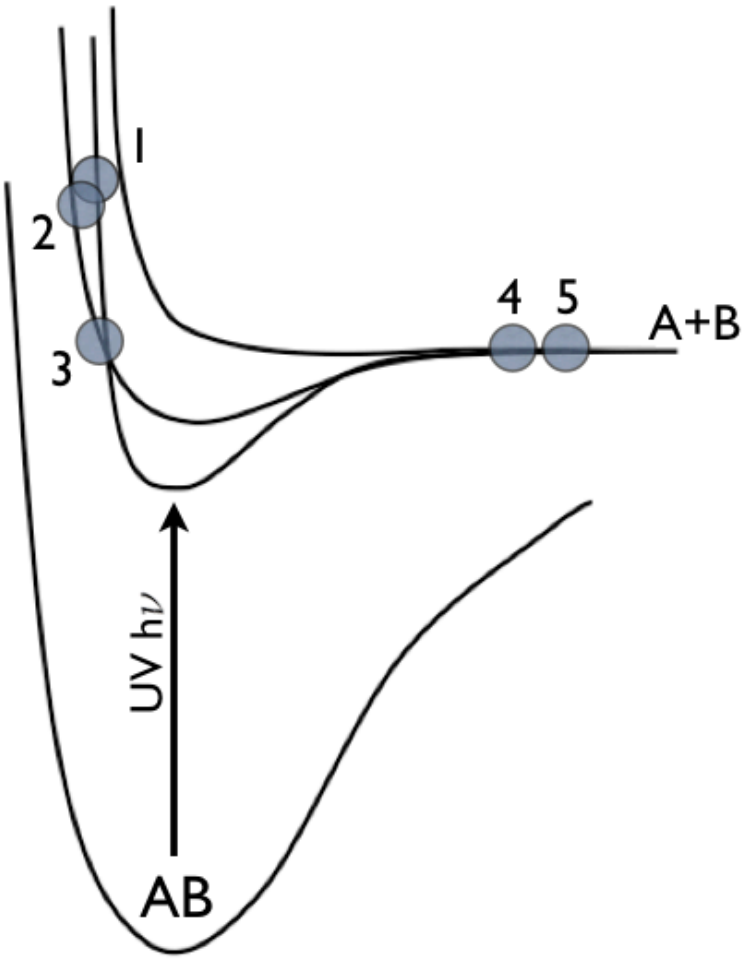

FIGURE 1.3: 1) Symmetry of excited electronic state; 2) Coherent excitation of multiple electronic states; 3) Nonadiabatic transitions at avoided crossings; 4) Nonadiabatic transitions at large internuclear separation; and 5) Coulomb interaction at large internuclear separation (adapted from Ref 38).

1.2 Scope of this Thesis

This thesis is organized as follows: Chapter 2 includes relevant background on the H atom, its significance in the emergence of quantum mechanics, in addition to a brief history of previous experimental efforts to measure the velocity-dependent H atom spin-polarization. Chapter 3 outlines the laboratory-frame theoretical treatment used here to fully characterize the H atom spin-polarization, and how this translates to interpreting photodissociation dynamics. The SPH-RTOF technique

is detailed in Chapter 4, which involves two different H atom detection approaches and three different experimental geometries. Chapter 5 includes a detailed description of the apparatus constructed to carry out these experiments, in addition to the resolution and sensitivity achievable with this approach. Experimental results are discussed in Chapter 6, including the UV photodissociation of H(D)Br and complete characterization of the incoherent and coherent H atom spin-polarization. Conclusions and outlook are presented in Chapter 7. This includes interesting tri- and polyatomic systems for which to apply SPH-RTOF, in addition to theoretical insights from the perspective of gauge invariance theory.

SPIN-POLARIZED HYDROGEN ATOMS

2.1 The Hydrogen Atom

This dissertation was largely motivated by a desire to generalize these powerful vector correlation methods in photodissociation experiments through application to the H atom, a "universal photoproduct". The H atom also however has special significance in our interpretation of fundamental chemical principles as the simplest atomic system. The Bohr model accounted for the structure in the H atom spectrum but seemed nonsensical to many scientists at the time. One of its implications was space-quantization associated with the orbital motion of the electron around the nucleus.

Experimentally, Stern and Gerlach in 1922 successfully demonstrated this space quantization. Stern recognized that, according to this model, the space quantization should be only twofold, as the projection of the orbital angular momentum was limited to h/2p. The twofold character made feasible a decisive test of spatial quantization using magnetic deflection of an atomic beam [46]. In their seminal experiment, a beam of silver atoms was subjected to an inhomogeneous magnetic field. Classical mechanics predicted that the atomic magnets would precess in the field, but remain randomly oriented, so the deflections would only broaden, but not split the beam [46]. However, Stern and Gerlach experimentally observed the single beam split into two distinct components, one which pointed in the direction of + Z, and one in the direction of - Z, after passing through the inhomogeneous

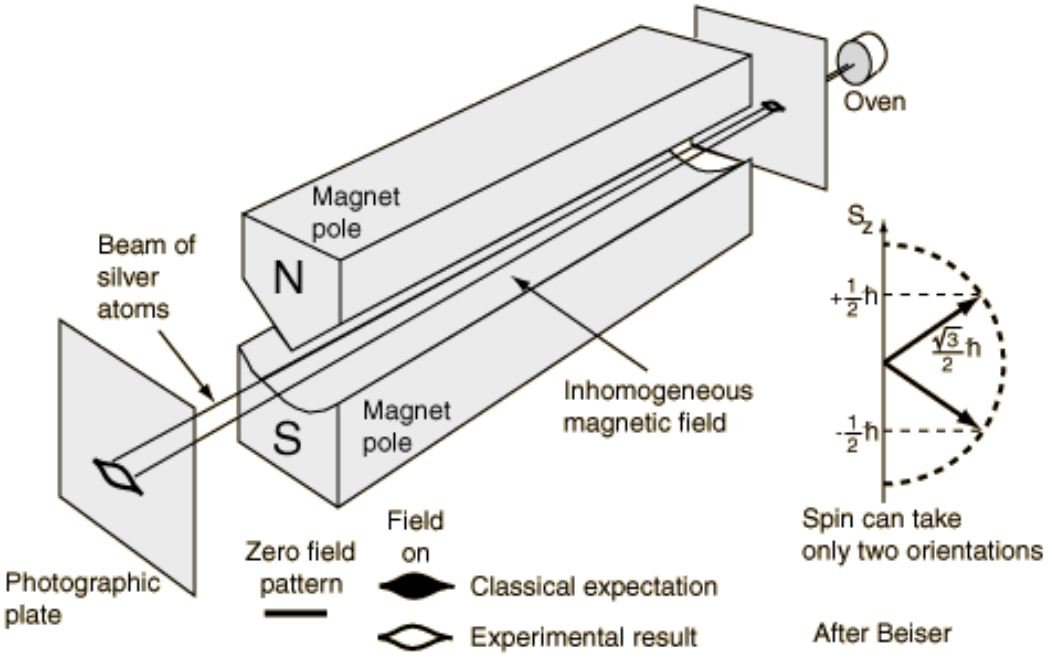

FIGURE 2.1: Stern-Gerlach experiment revealing the intrinsic angular momentum in the electron from reference [1]

.

magnetic field. Ironically, silver atoms have no orbital angular momentum, and would exhibit no associated space-quantization. It was only recognized five years later that this behavior was the result of an intrinsic angular momentum of the electron, independent of its orbital angular momentum [46]. This experiment is illustrated in Figure 2.1 below.

The doublets seen in the atomic spectra of alkali atoms were the first indication of a missing degree of freedom not accounted for in the emerging quantum theory. Pauli then introduced this in an ad hoc manner, forming the basis for the Pauli exclusion principle which is of profound importance, even in modern quantum chromodynamics [47]. It was not until Dirac combined relativity with quantum mechanics that spin emerged naturally as a product of the theory [48].

The state-selective experiments described here use polarized light to probe fundamental dynamical processes through direct measurement of the velocity dependent H atom spin-polarization. However, laser fields alone cannot directly interact with spin; instead, a magnetic field is required. The use of large magnets in the Stern-Gerlach approach is cumbersome, and not conducive to the state-selective molecular beam experiments used today. Today, spin-polarized beams are widely produced for studies of things such as anti-hydrogen [49] and characterized using a Breit-Rabi polarimeter [50]. This is an elaborate and expensive contraption, also not amenable to use in photodissociation studies. SPH-RTOF takes advantage of the spin-orbit interaction in the H atom 2p level to allow a laser-dependent probe that is spin-sensitive. In effect, we are using the orbital motion imparted to the electron during detection to create the necessary magnetic field needed. The following section describes the inherent difficulty of direct experimental measurement of the H atom spin, as well as previous experimental efforts to do so.

2.2 Production and Detection of Spin-Polarized Hydrogen Atoms: A Brief History

The production of spin-polarized hydrogen atoms (SPHs) in photodissociation of hydrogen halides was predicted over 30 years ago [51], [52]. Experimental determination of the H atom spin polarization has been pursued along various avenues in recent years. Important landmarks in this endeavor are briefly outlined below.

In the first reported SPH experiment by Rakitzis and coworkers, the angular distribution of the H atom photofragment spin polarization was not directly measured; instead, it was inferred from measurements of the angular momentum polarization of the Cl or Br cofragment in photodissociation of HCl and HBr [53], [3]. Subsequent to this work, the group utilized a (1+1) laser-induced fluorescence scheme in which VUV radiation was used to detect spin-polarized H atoms directly as shown in Figure 2.2 [2]. This experiment was inherently difficult as the use of a reflection polarizer in the detection system required the physical rotation of the entire detection system to measure the single incoherent anisotropy parameter induced by circularly polarized photdissociation light. Most recently, Rakitzis et al measured the spin-polarization of H atoms by (2+1) laser-induced flourescence, produced via the photodissociation of *thermal* HBr molecules with 193 nm light. This scheme involved two-photon laser excitation at 205 nm and fluorescence at 656 nm. Absorption of two circularly polarized photons and detection of linearly polarized fluorescence leads to complete m-state selectivity in the H-atom detection. However, the approach did not resolve the H atom recoil speed and thus could not disentangle the underlying Br and Br* contributions, although the results were shown to be consistent with inferences based upon other measurements. This setup is illustrated above, from Reference [2].

The lack of appropriate automatic angle-tuning for the tripling crystals in the above-described arrangement did not allow Rakitzis et al to maintain stable intensity of the 205 nm light over more than about 2.5 cm^{-1}, thus preventing them from obtaining the whole Doppler profile of the hydrogen atoms [2]. However, they were able to take a qualitative scan of half of the Doppler profile, shown in

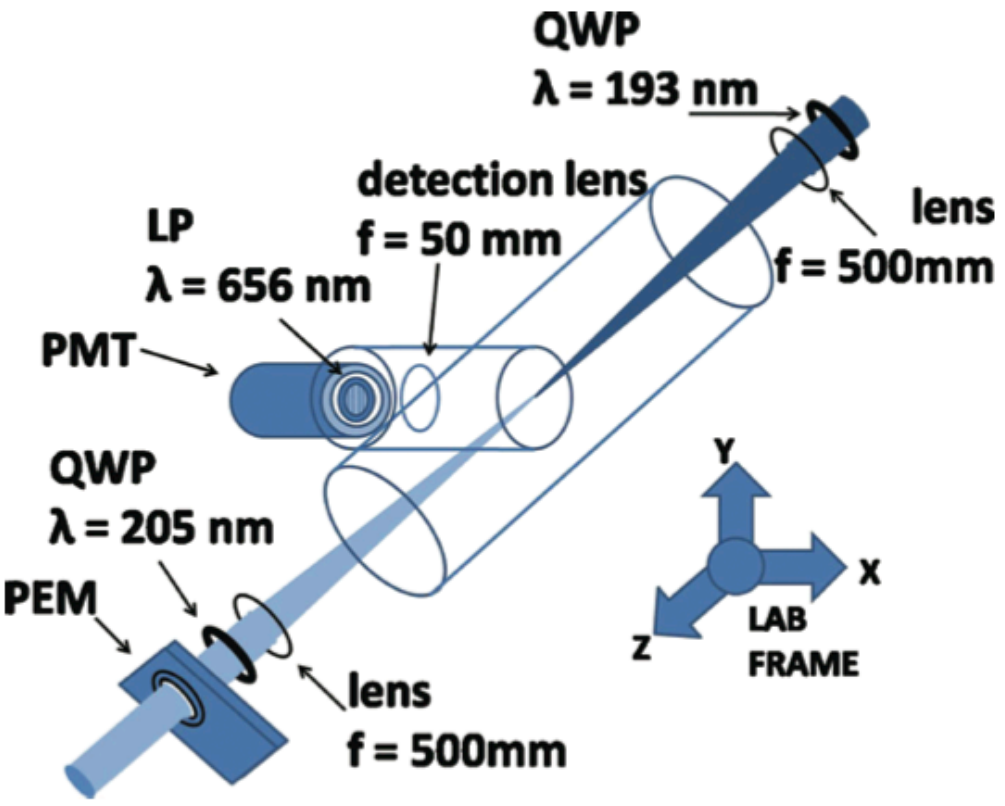

FIGURE 2.2: Schematic for Rakitzis experimental setup, from Reference [2].

the Figure 2.3 below, which shows that the peak of the Doppler profile is at the maximum velocity projection of the H atoms of about 23 km s^{-1} [2]. Also, the experiment suffered poor signal to noise given the thermalized conditions of the sample and the low sensitivity of the detection (Figure 2.4). It was necessary to monitor the degree of polarization as a function of bulb pressure to attempt to find nascent conditions. SPH-RTOF offers a means of measuring H atom spin polarization and its velocity dependence directly, overcoming many of the challenges associated with these earlier efforts.

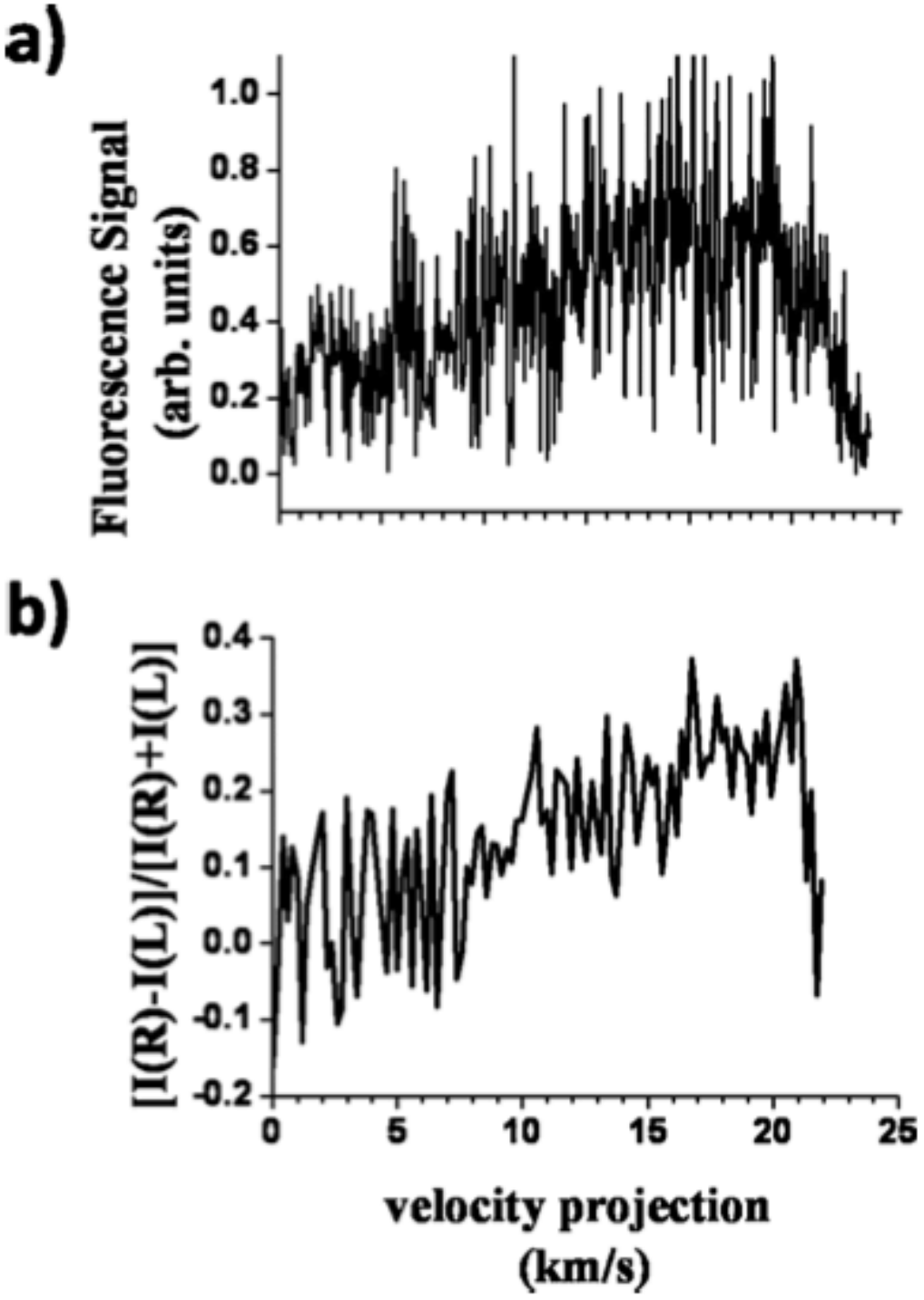

FIGURE 2.3: Rakitzis experimental results from (2+1) LIF detection scheme from Reference [2]. a) includes the relative fluorescence signal coming from H atoms having velocity projections with respect to the direction of the probe laser between 0 and 25 km per s (controlled by the energy of the dissociation photon). b) is the ratio of the difference/sum spectra using right and left circularly-polarized probe light.

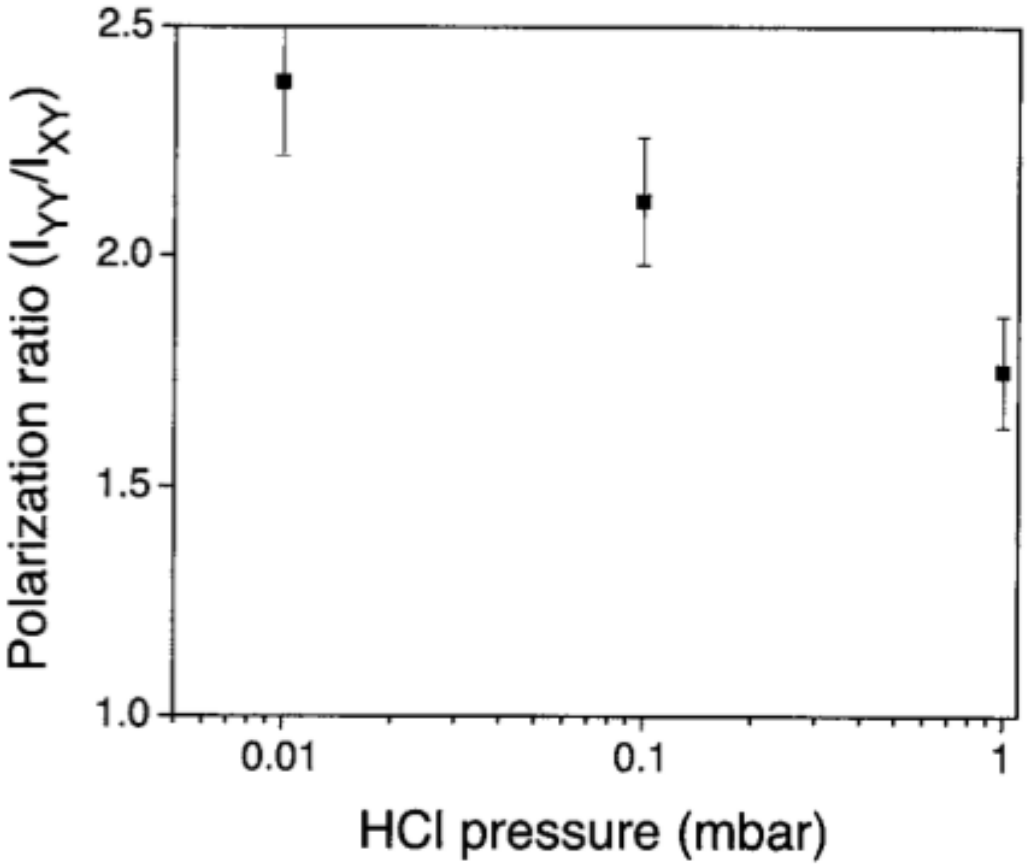

FIGURE 2.4: Measurement of the polarization ratio as a function of HCl pressure by Rakitzis et al from Reference. [3]. At higher pressures, the ratio of spin polarization decreases from the ideal value of 2.5, indicating depolarization from collisions.

CHAPTER 3

THEORY: SPIN-POLARIZATION OF ATOMIC PHOTOFRAGMENTS

3.1 Laboratory frame-theoretical treatment

This dissertation utilizes the laboratory-frame treatment by Vasyutinskii and coworkers to describe the orientation of hydrogen atoms produced in photodissociation [54]. In the case of the diatomic dissociation AB + hν $\rightarrow$ A + B, the two fragments have angular momenta j_A and j_B, respectively. Here, the differential excitation cross-section matrix elements ${\sigma^{(j_A)}}_{m'm}(\theta, \phi)$ give the probability of photofragment A flying in a direction specified by the polar angles θ and ϕ with components m, m' of j_A along the space-fixed Z axis [4]. This reference frame is given in Figure 3.1 below.

The diagonal elements of the matrix ($m = m'$) give the probability of producing the fragment with a specific angular momentum j_A and component m, while the off-diagonal elements ($m \neq m'$) describe the coherence between states with different m quantum numbers [55]. The initial and final total angular momenta of the molecule are J_i and J, respectively.

The differential cross section matrix elements given above can then be expressed in terms of the angular momentum polarization irreducible cross sections, ${\sigma^{(j_A)}}_{KQ}(\theta, \phi)$ $\equiv \sigma_{KQ}(\theta, \phi)$.

These are spherical tensors of rank K and component Q, where Q = -K ... K [55], [28], [56].

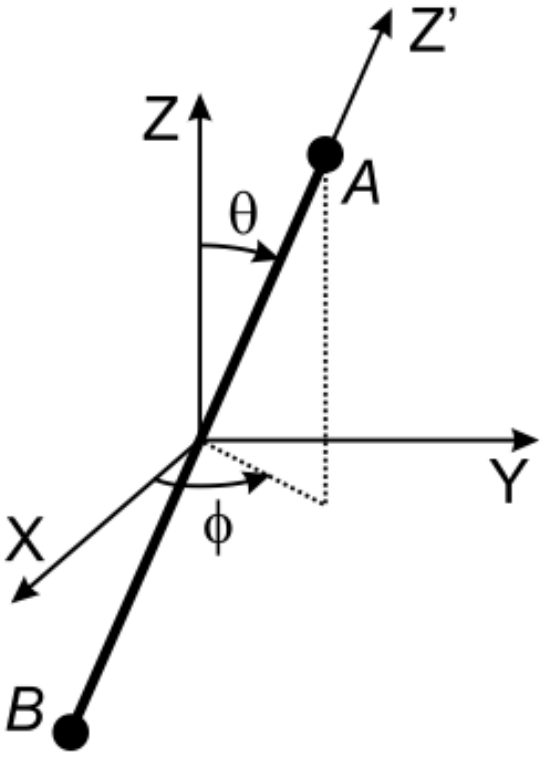

FIGURE 3.1: H atom rank K = 1 laboratory- frame orientation anisotropy parameters adapted from Reference [4].

$$\sigma_{KQ}(\theta,\phi) = \sum_{m',m}(-1)^{j-m}(2\mathrm{K}+1)^{1/2} \begin{pmatrix} \mathrm{j}_A & \mathrm{j}_A & \mathrm{K} \\ \mathrm{m} & \text{-m'} & \text{-Q} \end{pmatrix} \sigma^{(j_A)}{}_{KQ}(\theta,\phi) \qquad (3.1)$$

The photofragment differential cross section given in eq. 3.1 for one-photon fragmentation in the axial recoil approximation [45] is:

$$\sigma_{KQ}(\theta,\phi) = \frac{3\sigma_0(2K+1)^{1/2}}{4\pi} \sum_{k_d,q_d,Q'} \sum_{q,Q'} (-1)^{K+q'} E_{k_d q_d}(e) \frac{f_K(q,q')}{f_0(0,0)+2f_0(1,1)}$$

$$\times(2k_d+1)^{1/2}\begin{pmatrix} 1 & 1 & \mathrm{k}_d \\ \mathrm{q'} & \mathrm{-q} & \mathrm{-Q'} \end{pmatrix} D^{K*}_{QQ'}(\phi,\theta,0)D^{k_d}_{q_dQ'}(\phi,\theta,0) \qquad (3.2)$$

The multipole rank K ranges from K = 0 to K = $2j_A$ [55]. Hydrogen atoms however are a rank K = 1 system, so only the K = 0 (photofragment density) and K = 1 (orientation) terms are discussed in this work. An important point and advantage of the state multipole treatment illustrated in eq. 3.1 above is that each fragment's irreducible photodissociation cross section (σ_{KQ}) can be treated separately from all others [22]. Furthermore, each cross section σ_{KQ} has a distinct angular distribution which is evident experimentally. The values $f_K(q,q')$ are *dynamical functions*, which contain all of the information on the transition dipole moments and fragmentation dynamics [4]. The full quantum mechanical photodissociation experiment is given by determination of all independent photofragment cross sections (state multipoles); thus, all quantum mechanical amplitudes and phases are given from this theory [26], [36].

The fragment state multipoles $\rho_{KQ}(\theta,\phi)$ more conveniently describe the photofragment polarization cross sections given by eq. (3.1)

$$\rho_{KQ}(\theta,\phi) = \frac{\sigma_{KQ}(\theta,\phi)}{(2j_A+1)^{1/2}\sigma_0} \qquad (3.3)$$

The H atom K = 1 fragment state multipole is directly proportional to the fragment dipole, and is related to the fragment orientation parameter $\mathrm{A}_{KQ}(\theta,\phi)$ in

the following way [28]:

$$A_{1Q} = \frac{1}{\sqrt{3}} \frac{Re[\rho_{1Q}]}{\rho_{00}} \tag{3.4}$$

One can therefore obtain expressions for a single differential photofragment state multipole utilizing eqns. (3.3) and (3.4) above [28].

The laboratory-frame theoretical foundation for the geometries relevant to this work is described in the following sections within the context of the convenient state mutipole treatment. The photofragment angular distributions for rank K = 0 - 1 only are considered here, as there is no quadrupole moment associated with the H atom to exhibit the alignment described by the rank K = 2 state multipole found in larger atomic species.

3.1.1 Angular Contribution from K = 0 State Multipole

The overall spatial anisotropy discussed in Chapter 1 of this work is described by the zeroth order dynamical function β_0 in the state multipole treatment [45]. Two different time-of-flight geometries are needed to determine the angular contribution of the K = 0 state multipole. The first is linearly polarized dissociation light along the Z axis.

$$\rho_{00}(\theta,\phi) = \frac{1}{4\pi\sqrt{2j_A+1}}[1+\beta_0 P_2(\cos\theta) \tag{3.5}$$

While the second is linearly polarized dissociation light along the Y axis.

$$\rho_{00}(\theta,\phi) = \frac{1}{4\pi\sqrt{2j_A+1}}[1-\frac{\beta_0}{2}(1-3\sin^2\theta\sin^2\phi)] \tag{3.6}$$

The overall spatial anisotropy can then be described in dynamical terms *via* eq. 3.7 [54]

$$\beta_0 = \frac{2[f_0(0,0)-f_0(1,1)]}{f_0(0,0)+2f_0(1,1)} \tag{3.7}$$

3.1.2 Photofragment Orientation for K = 1 State Multipole

For a K = 1, Q = 0, ±1 system, three parameters in three different geometries are needed to fully describe the photofragment orientation [4].

Geometry I: Coherent orientation parameter induced by right or left-circularly polarized photolysis light, γ_1 [4]

$$\rho_{10}(\theta,\phi) = -\frac{3\sqrt{3}}{4\pi\sqrt{2}\sqrt{2j_A+1}}[\alpha_1 \cos^2\theta + \frac{\gamma_1}{2}\sin^2\theta], \tag{3.8}$$

$$\rho_{11}(\theta,\phi) = -\frac{3\sqrt{3}}{4\pi\sqrt{2}\sqrt{2j_A+1}}\sin\theta\cos\theta e^{i\theta}[\alpha_1 - \frac{\gamma_1}{2} - \frac{i\gamma_1'}{2}] \tag{3.9}$$

Geometry II: Coherent orientation parameter induced by linearly polarized photolysis light, γ_1' [4]

$$\rho_{10}(\theta,\phi) = -\frac{3\sqrt{3}}{8\pi\sqrt{2}\sqrt{2j_A+1}}\gamma_1'\sin^2\theta\sin 2\phi, \tag{3.10}$$

$$\rho_{11}(\theta,\phi) = -\frac{3\sqrt{3}}{4\pi\sqrt{2}\sqrt{2j_A+1}}\gamma_1'\sin\theta\cos\theta\sin\phi \tag{3.11}$$

Geometry III: Incoherent orientation parameter induced by circularly polarized photolysis light, α_1 [4]

$$\rho_{10}(\theta,\phi) = 0, \tag{3.12}$$

$$\rho_{11}(\theta,\phi) = -\frac{3\sqrt{3}}{4\pi\sqrt{2}\sqrt{2j_A+1}}\gamma_1'\sin\theta\cos\theta i e^{i\theta} \tag{3.13}$$

These photofragment anisotropy parameters are also normalized first-order dynamical functions [54]:

$$\gamma_1 = \frac{2Re[f_1(1,0)]}{f_0(0,0) + 2f_0(1,1)} \tag{3.14}$$

$$\gamma_1' = \frac{2Im[f_1(1,0)]}{f_0(0,0) + 2f_0(1,1)} \tag{3.15}$$

$$\alpha_1 = \frac{f_1(1,1)}{f_0(0,0) + 2f_0(1,1)} \tag{3.16}$$

Each parameter arises as a result of distinct features of the photodissociation event. γ_1 represents contribution to the photofragment orientation from coherent excitation of a parallel and perpendicular transition. γ_1' also describes the coherent excitation of a parallel and perpendicular transition, but it contributes only to the part of the fragment orientation that is produced by linearly polarized photolysis light and vanishes after averaging over all recoil angles [4]. Finally, α_1 represents contribution from incoherent excitation through perpendicular transitions.

These well-defined parameters nicely correspond to practically observable measurements with distinct angular distributions. These are summarized in Figure 3.2 below. Moreover, a single parameter is acquired at a given time, such that contributions to the photofragment orientation from incoherent and coherent processes induced by linear and circularly-polarized photolysis may be disentangled

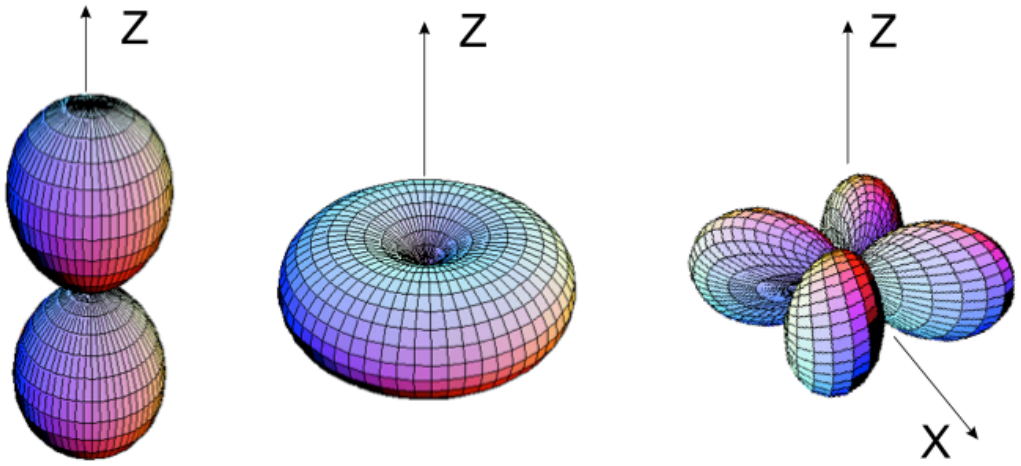

FIGURE 3.2: H atom rank K = 1 laboratory- frame orientation anisotropy parameters from Reference [4].

in a straightforward fashion.

CHAPTER 4

EXPERIMENTAL APPROACH

4.1 Experimental Overview

We employ two different approaches, both based on the same 2-color double-resonance excitation scheme in order to obtain the three parameters required to measure the H atom spin polarization. The characteristic angular distributions of each of the three parameters are conceptually presented in Figure 4.1 below [4]. The two coherent parameters γ_1 and γ_1' are obtained with the widely-employed Rydberg "tagging" approach [57]. Here, detection occurs perpendicular to the laser propagation direction, where these coherent contributions to the spin polarization may be captured without scanning the probe laser. On the other hand, the α_1 spin polarization vanishes perpendicular to the probe laser propagation direction, but reaches a maximum parallel to it and thus cannot be measured in the same convenient Rydberg tagging geometry. However, we demonstrate that this same double-resonance excitation scheme can be employed in an ion-imaging approach where prompt field-ionization occurs in the interaction region.

Three aspects of the experiment are necessary for this approach to work: (1) the spin-polarization angular distributions for the three parameters are disjoint; that is, specific recoil directions in particular probe geometries are sensitive only to one parameter at a time; (2) the double-resonance excitation scheme described below is spin-sensitive if a single fine structure component can be isolated; (3) the Rydberg time-of-flight approach can readily achieve a Doppler selectivity of 3% for the

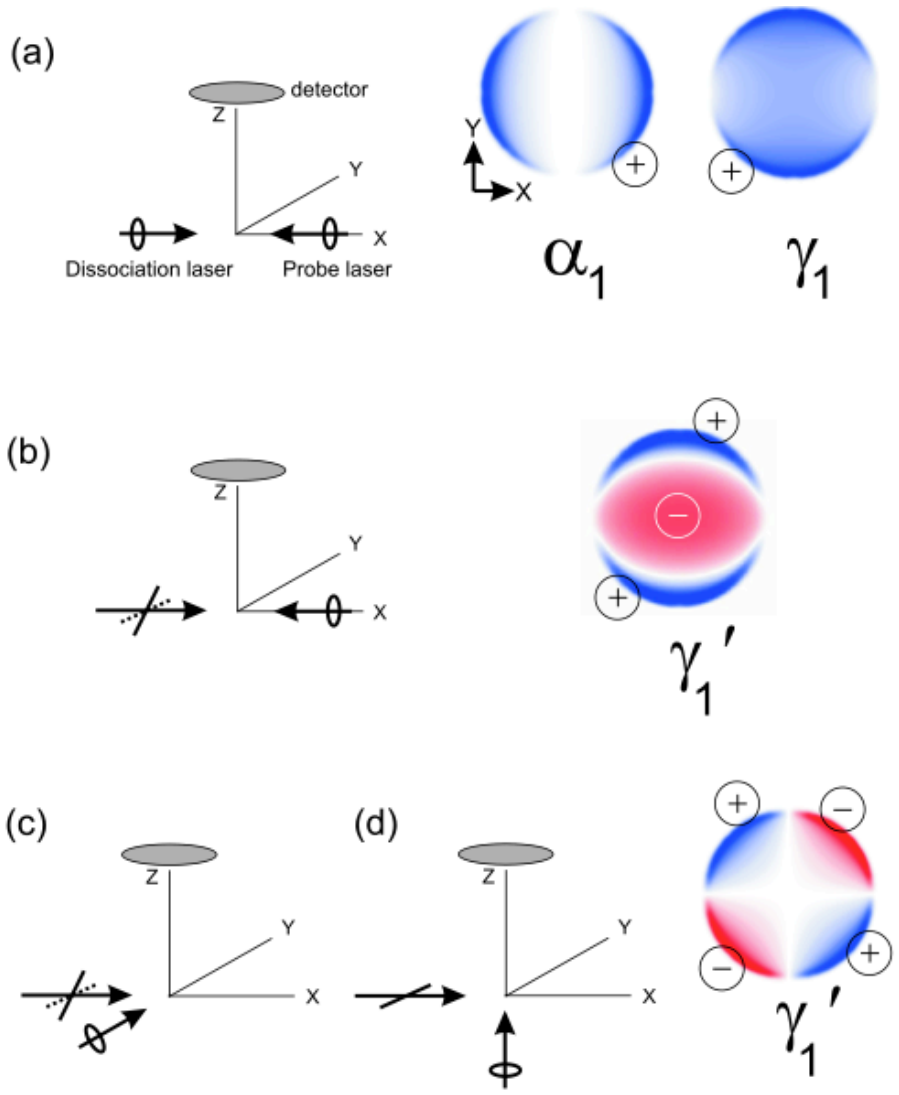

FIGURE 4.1: Orientation image basis functions in four different geometries with associated orientation parameters taken from Ref 17 of this work.

fastest fragments, which is more than enough to ensure the needed fine structure selectivity if either of the two excitation lasers are narrow enough in line width to achieve this as well [37]. The traditional Rydberg tagging approach in addition to the prompt field-ionization ion imaging geometry nicely satisfy these conditions. An introduction to Rydberg tagging, ion imaging, and our modification to both techniques is described below. This includes a unique doube-resonance excitation scheme and three distinct experimental geometries.

4.2 Hydrogen Rydberg Time-of-Flight Overview

The SPH-RTOF approach is based upon the widely-employed Rydberg tagging technique pioneered by Welge and coworkers [57]. Although other techniques including ion imaging are, in a sense, more universal, Rydberg "tagging" holds a special place owing to the remarkable resolution and sensitivity the method affords, and the broad importance of hydrogen atoms as photoproducts for dissociation of countless molecules. The key feature of the technique is the efficient two-step excitation of the nascent H-atom from its ground state to a Rydberg state with a high principle quantum number, n. The H atom here is not directly ionized by the probe beam as is the case with more conventional TOF methods (see Figure 4.3). Instead, the H atoms are tagged in the interaction region and fly as neutrals through a field-free time-of-flight region. A small field of approximately 10 V/cm is applied in the interaction region, which eliminates any unwanted prompt ions, and also induces l-mixing in the H atom resulting in long lifetimes (on the order of milliseconds) of the high-n Rydbergs [58]. The long-lived Rydberg atom flies as a neutral 30 -75 cm away at which point it reaches a detector and is subsequently field ionized and counted as a function on flight time.

The figures below summarize the above aspects of this technique. Figure 4.2 illustrates the general experimental scheme wherein a molecular beam is intersected by three lasers serving to dissociate, excite, and "tag" the nascent H atoms. The detector resides perpendicular to both the lasers and the molecular beam. The 2-step excitation in contrast to the conventional Resonance-Enhanced Multiphoton Ionization (REMPI) approach is given in Figure 4.3. Finally, the H atom Rydberg

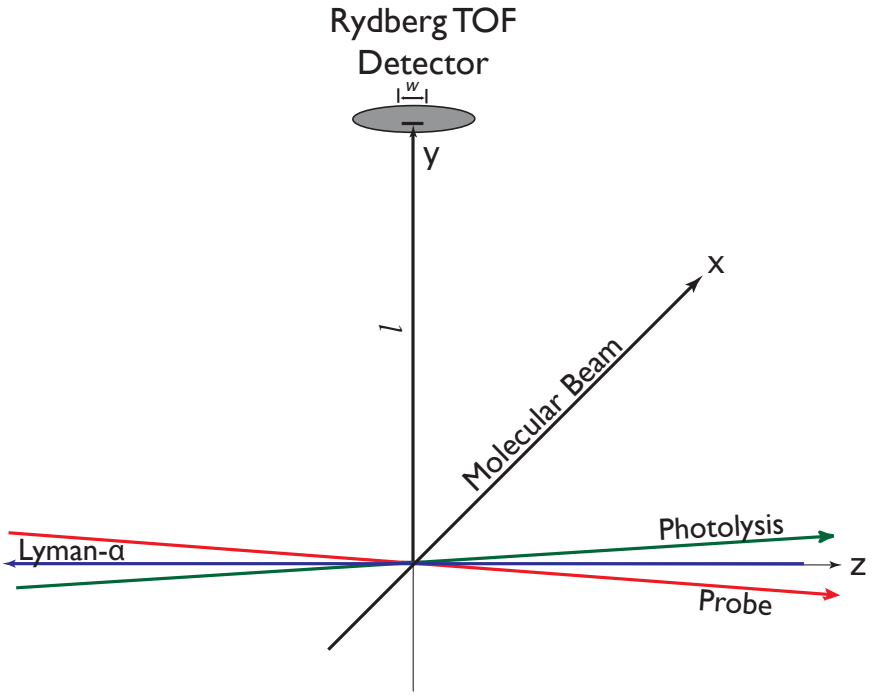

FIGURE 4.2: General Rydberg tagging experimental geometry. Three counter-propagating lasers and detection perpendicular to the molecular beam is employed.

transition spectrum is shown in Figure 4.4. Rydberg tagging generally involves excitation to high-n Rydberg states for n = 20 to n = 80, although any high-n Rydberg behaves similarly [57].

Excitation from the H atom ground state takes the following course:

$$\mathrm{H(n = 1)} + h\nu\ (\lambda = 121.6\ \mathrm{nm}) \rightarrow \mathrm{H\ (n{=}2)}$$

$$\mathrm{H(n = 2)} + h\nu\ (\lambda = 365\ \mathrm{nm}) \rightarrow \mathrm{H\ (n \sim 80)}$$

The H atom n = 1 to n = 2 excitation requires production of Lyman-α radiation, in the vacuum ultra-violet. There are a number of ways to achieve this including frequency tripling [59], sum-difference frequency mixing [60], and difference mixing in various noble gases [60]. This work relies on frequency tripling in a Kr gas cell to produce Lyman-α radiation, which has a huge absorption cross section

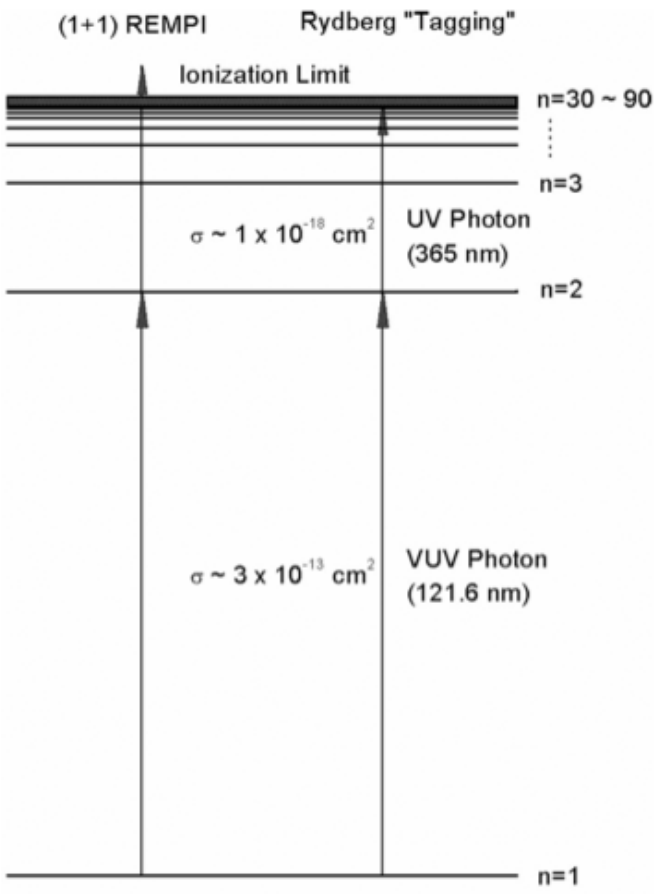

FIGURE 4.3: REMPI versus Rydberg tagging detection from Reference [57].

of $3.0\times\ 10^{-13} cm^2$. A complete description of this process is given in Chapter 5. Following excitation to n = 2, the H atom is excited to a high-n state just below the ionization threshold with $\sim$ 365 nm radiation. Spatial and temporal overlap of the excitation and tagging probe beam are essential in this approach. The tagged H atoms that fly toward the detector are ultimately field-ionized at the detector and counted. Because H atoms move very fast relative to the parent molecular beam, the beam velocity spread contributes relatively little to the uncertainty in the velocity measurement. Futhermore, as a neutral atom, the Rydberg is not sensitive to stray fields that could also undermine an accurate time-of-flight determination for an ion [38]. Finally, because this relies on a double-resonance excitation with extremely large cross sections, and detection of the energized particle long after

the laser has fired, it is essentially a zero background measurement.

Our variation of this method involves the use of polarized lasers in specific geometries, and is built on the recognition that Rydberg tagging can enforce the strict Doppler selection that allows for isolation of a signle fine structure component in detection which is necessary to achieve a spin-sensitive probe. Furthermore, it is also the case that these experimental geometries completely isolate the three anisotropy parameters needed to determine the full angular and speed dependence of the H atom and its spin polarization, allowing an accurate determination of each of these in turn [37].

4.3 Velocity-Mapped Ion Imaging

The ion-imaging technique, as first introduced by Chandler and Houston [61], [62], and the high-resolution, velocity mapping variant developed by Eppink and Parker [63], [64] have become widely used in studies of molecular photodissociation and reactive scattering [54], [23]. In contrast to the time-of-flight method, the ion imaging technique extracts both kinetic energy and angular distribution information from the spatial appearance of a single image. It enjoys "4π" collection efficiency, as opposed to the 10^{-4} collection efficiency of Rydberg tagging. In this technique, a time-of-flight mass spectrometer is combined with a two-dimensional (2D) position-sensitive detector, a microchannel plate (MCP) coupled to a fast phosphor screen and a charge coupled device (CCD) camera [65]. The photofragment ion cloud is prepared in the interaction region which in the velocity-mapped imaging

approach includes focusing lenses with varying biases so as to optimize the velocity resolution of the data acquired. This setup is illustrated in Figure 4.4 below. Once the photofragment ion cloud has emerged from the ion optics arrangement, it expands through a time-of-flight region toward a position-sensitive microchannel plate (MCP)/phosphor screen detector coupled to a CCD camera. Here, the three-dimensional (3D) spatial distribution of the photofragment is projected onto a two-dimensional (2D) surface; all particles of the same initial velocity vector are mapped onto the same point on the detector [64]. The 2D image is recorded and is then transformed so as to reconstruct the original full 3D photofragement spatial distribution using inverse Abel transformation or related methds. In doing so, the complete velocity and angular distributions for a given process may be extracted from a single image. More recent approaches rely on time-slicing of the ion cloud as it reaches the detector in order to record the velocity distributions directly without need for reconstruction [65]. These approaches are challenging for H atoms but some success has been achieved.

The ion imaging detection method is utilized in SPH-RTOF to measure the incoherent H atom spin-polarization induced by circularly polarized photolysis light. The angular distribution of the orientation here is maximum along the probe laser propagation direction and can thus be captured utilizing the ion imaging approach described above. While all three parameters can be acquired in a single geometry with ion imaging, scanning the probe laser to include the entire Doppler width of the H atom photofragments is necessary. This issue is further addressed below.

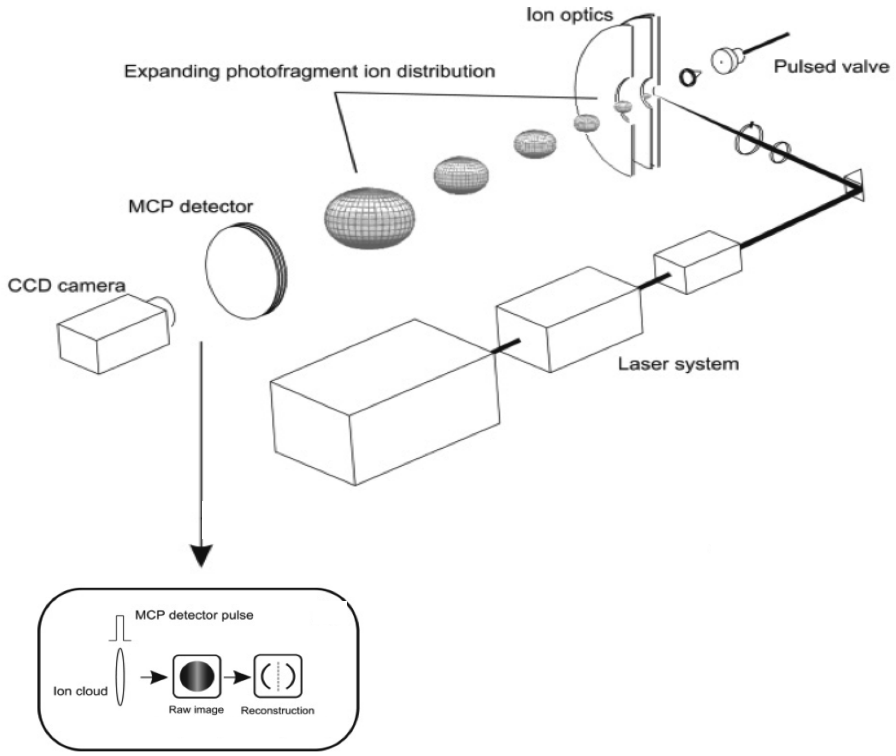

FIGURE 4.4: Velocity-mapped imaging configuration from Reference [5].

4.4 Spin-Polarized Hydrogen Rydberg Time-of-Flight

The basis of the SPH-RTOF technique and the related imaging method we employ is a double-resonance excitation scheme, used in three experimental geometries. The combined use of Rydberg tagging and pulsed-field ionization velocity mapped imaging allow us to obtain the complete description of the H atom photofragment spin polarization and its velocity dependence. The double-resonance excitation and experimental geometries are described in the following sections.

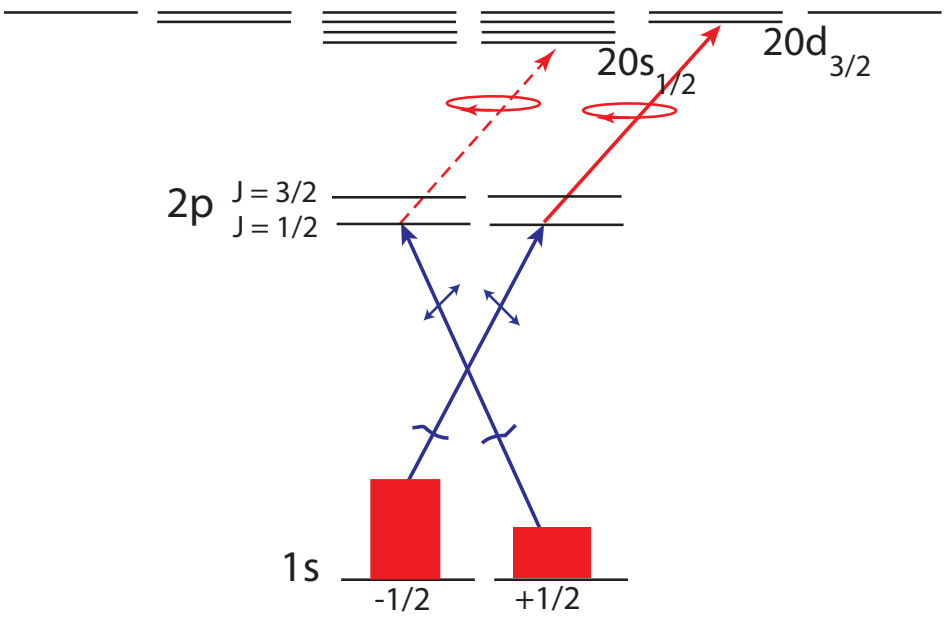

FIGURE 4.5: SPH-RTOF double-resonance excitation scheme shown with linearly-polarized Lyman-α excitation, and RCP probe.

4.5 SPH-RTOF Double-Resonance Excitation

The spin-sensitive detection scheme is summarized in Figure 4.5. The ground state H atom magnetic sublevels, shown with distinct populations as might be produced in a general photodissociation event, are excited by a linearly polarized laser at 121.6 nm (Lyman-α). The direction of this polarization is not important given the counterpropagating laser configuration employed here [38]. The propagation direction of the circularly polarized tagging probe beam defines the quantization axis, and in this frame the selection rules for the Lyman-α excitation are $\Delta m = \pm 1$. The laser is tuned to line center for the $2p_{1/2}$ fine structure energy state. Spin selectivity comes in the tagging step, which is illustrated in Figure 4.5 for RCP probe light.

There are two possible excitation pathways: $1s_{1/2} \rightarrow 2p_{1/2} \rightarrow 20s_{1/2}$ or $20d_{3/2}$. However, the radial integrals for transitions to the $20s_{1/2}$ Rydberg state are much

smaller than to the $20d_{3/2}$, so we neglect that contribution [37]. This leads to a very simple result. The absorption intensity I is given by:

$$I_r \approx C\left(\rho_{00} - (\rho_{10}/2)\right), \tag{4.1}$$

where $\rho_{00} = \rho_{00}^{1/2}$ and $\rho_{10} = \rho_{10}^{1/2}$ are H atom $1s$ ground state state multipoles which are given by:

$$\begin{aligned} \rho_{00} &= (1/\sqrt{2})\left(N_{1/2} + N_{-1/2}\right) \\ \rho_{10} &= (1/\sqrt{2})\left(N_{1/2} - N_{-1/2}\right), \end{aligned} \tag{4.2}$$

where $N_{1/2}$ and $N_{-1/2}$ are the H-atom m-state populations.

The spin polarization degree is given by

$$< s_Z >= \frac{\rho_{10}}{\rho_{00}} = \frac{N_{1/2} - N_{-1/2}}{N_{1/2} + N_{-1/2}}. \tag{4.3}$$

The Lyman-α light in eq. 4.1 is assumed to propagate along the $-Z$-axis. The 366 nm light is assumed to be RCP propagating along $+Z$-axis. If it is LCP, the sign in the second term in eq. 4.1 should be replaced by (+) [37]. C is a constant that depends on the both beams intensities and on the reduced transition matrix elements. The result in eq.4.1 is approximate because the intensity of the transition $2p \rightarrow 20s$ has been neglected compared to the intensity of the transition $2p \rightarrow 20d$.

In case of the excitation via the $2p_{3/2}$ fine structure energy state the tagging intensity I_r is given by:

$$I_r \approx 2C\left((11/10)\rho_{00} + (\rho_{10}/2)\right). \tag{4.4}$$

C is the same constant as in eq. 4.1. The result in eq. 4.4 is also approximate for the same reason as the signal in eq. 4.1, and the 366 nm light is assumed to be RCP propagating along the $+Z$-axis. Moreover, within the level of accuracy employed the factor 41/40 in eq. 4.4 may be set to 1.

4.4.2 SPH-RTOF Experimental Geometries

In addition to the spin-sensitive double-resonance excitation scheme employed in SPH-RTOF, three distinct geometries are further required to determine the orientation in the hydrogen atom. These geometries exploit the distinct angular distributions of the photofragments, and are derived from the state multipole treatment previously outlined in Chapter 3.

The counterpropagating laser arrangement (see Figure 4.2) is employed in each of the three geometries, where the quantization axis, Z, is defined by the propagation direction of the tagging probe beam. The dissociation laser propagates within 6^o of the direction of Z, whereas Lyman-α propagates along -Z. However, the axis of detection varies amongst the coherent and incoherent parameters measured in SPH-RTOF. The two coherent parameters γ_1 and γ_1' have angular distributions that reach a maximum perpendicular to the probe laser propagation direction,

which can be viewed in the conventional Rydberg tagging detection scheme along Y. The experimental geometries of γ_1 and γ_1' differ only in terms of the polarization of the photolysis light. γ_1 requires right and left circularly polarized light, whereas γ_1' requires linearly polarized light at $\pm 45^o$ [4]. Figure 4.6 summarizes these two geometries as well as the characteristic angular distributions of each.

The laboratory TOF signals may be directly converted to the speed-dependent orientation anisotropy parameters as follows [37]:

For Geometry I:

$$\frac{I_r - I_l}{I_r + I_l} = -\frac{3\sqrt{3}\,\gamma_1}{4 - \beta} \tag{4.5}$$

Similarly, for Geometry II,

$$\frac{I_r - I_l}{I_r + I_l} = -\frac{3\sqrt{3}\,\gamma_1'}{4 + \beta} \tag{4.6}$$

.

The experimental geometry associated with the incoherent parameter α_1 is quite different from those required to measure γ_1 and γ_1'. The Rydberg tagging geometry is blind to α_1 which vanishes perpendicular to the photolysis laser propagation direction. However, α_1 has a maximum along Z, and can be conveniently captured in the ion imaging geometry described in Section 4.3 above. The double-resonance excitation scheme remains unchanged in this configuration. However, the pulsed field ionization occurs in the interaction region long after (approximately 150 ns)

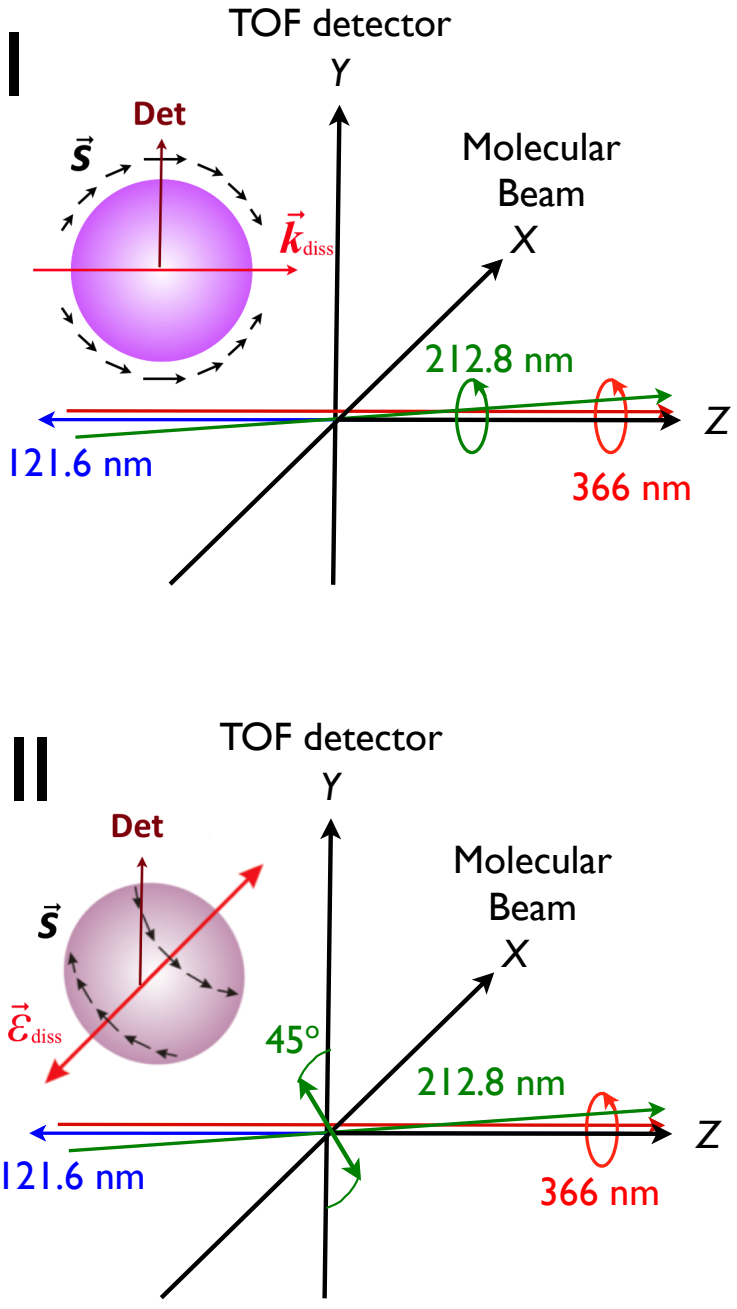

FIGURE 4.6: SPH-RTOF experimental geometry. γ_1 and γ_1' are obtained with $\pm 45^o$ linearly polarized photolysis and R/L circularly polarized photolysis, respectively. The Lyman-α beam is linearly polarized while the tagging probe is circularly polarized in all experiments.

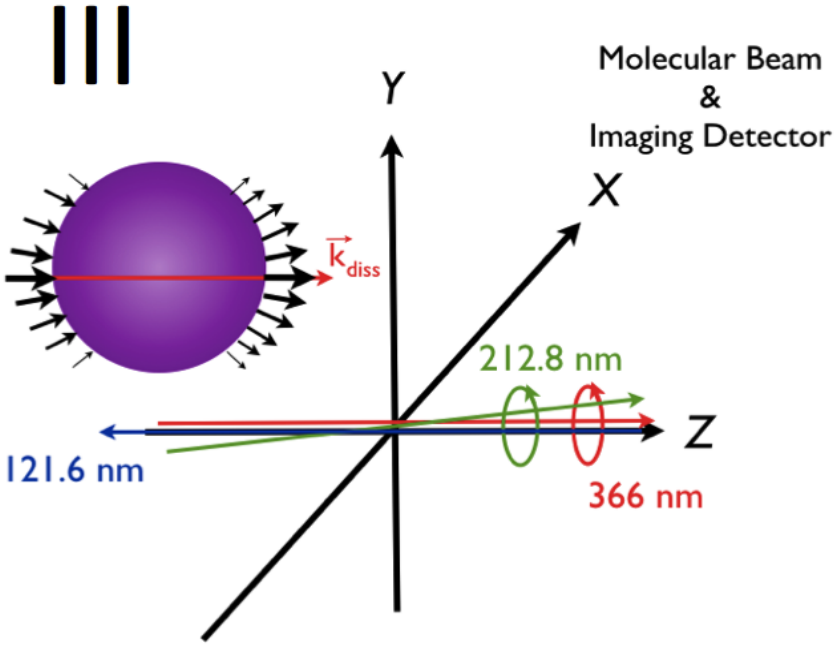

FIGURE 4.7: SPH-RTOF experimental geometry. α_1 and γ_1' is obtained with R/L circularly polarized photolysis, respectively. The Lyman-α beam is linearly polarized while the tagging probe is circularly polarized in all experiments.

the tagging probe beam selects a single spin state, and prior to entering the time-of-flight region. Extreme care is taken experimentally to ensure this brief ionization pulse occurs sufficiently long after the probe beam, as the presence of any stray fields in the interaction region can broaden the Rydberg transition which would no longer permit spin-selective detection. The precise arrangement is detailed in Chapter 5 here. One can easily verify that broadening of a Rydberg transition has not occurred as a consequence of the pulsed-field ionization in the interaction region by scanning the tagging laser. In a system with known spin-polarization, the experimental s_z will maintain the same magnitude, but will change sign upon variation of probe helicity. It should be noted that all three parameters can be viewed in this ion imaging geometry; however, scanning of the probe laser and dc slice imaging is needed to disentangle the contribution from each.

The conversion from TOF to the speed-dependent orientation anisotropy parameter α_1:

Geometry III:

$$\frac{I_r - I_l}{I_r + I_l} = -\frac{3\sqrt{3}\,\alpha_1}{2-\beta}. \tag{4.7}$$

Equations (4.1) and (4.4) show that the sensitivity to the H-atom spin polarization is the same with both probe transitions, however the signs are opposite to each other. This may be understood intuitively if we recognize that our spin-sensitivity arises from the spin-orbit interaction. According to the vector model, the total angular momenta of the first and the second spin-orbit states can be presented in the form: $\mathbf{j} = \mathbf{L} \pm \mathbf{S}$, where the signs (+) and (-) are related to j = 3/2 and j=1/2, respectively [44]. Therefore, by changing the probe transition we are effectively changing the sign of sensitivity to the ground state spin polarization.

Moreover, as shown in eqs. (4.1) and (4.4), the tagging signal intensity is twice larger in channel (2) than in channel (1). Performing summation of eqs. (4.1) and (4.4) it is easy to see a residual sensitivity of the ground state spin polarization of about 1/3 of what we expect on the $2p_{1/2}$ and $2p_{3/2}$ [37]. However, this result does not contradict the statement given above that the signals are equal and opposite because it is obtained without taking into account the coherence between the $2p_{1/2}$ and $2p_{3/2}$ states. This coherence may or may not be detected depending on the experimental conditions.

These results imply that if we have a system that shows spin polarization, and we

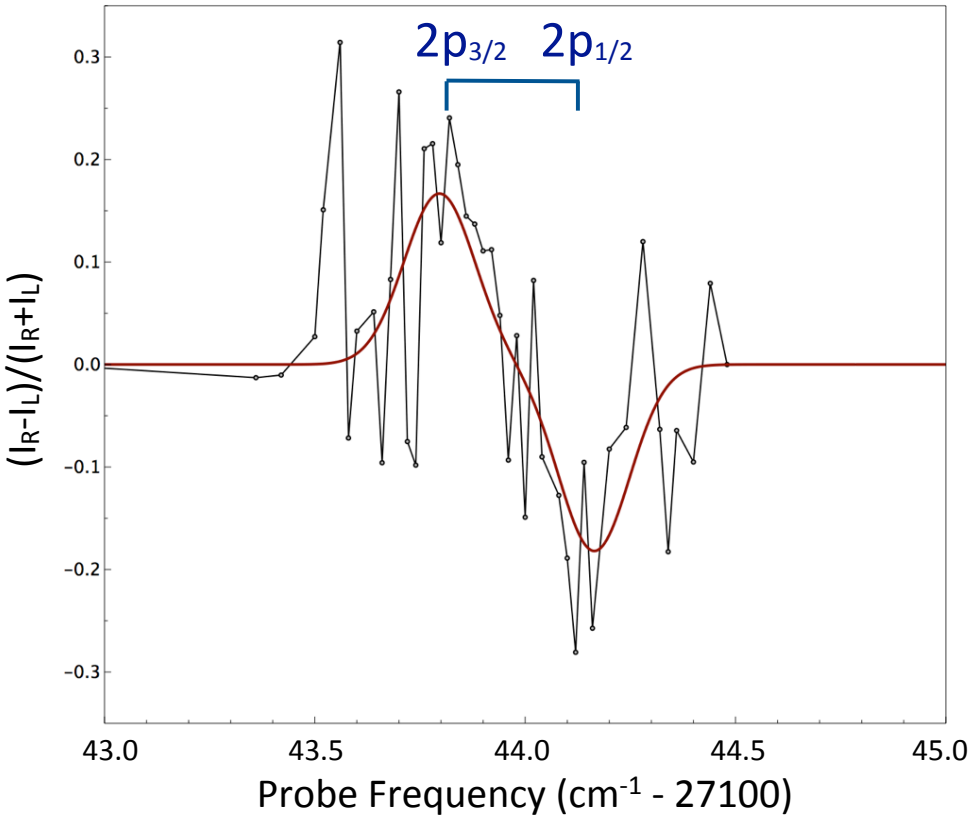

FIGURE 4.8: (I_r - I_l) / (I_r + I_l) for HBr $\rightarrow$ H + Br*($^2P_{1/2}$) at 213 nm plotted vs. tagging laser frequency. Solid line is a Gaussian fit with the centers fixed at the known 0.36 cm^{-1} splitting between the levels.

scan the tagging probe laser over this transition, we should see this sign change. As discussed in detail below and in reference [37], the UV dissociation of HBr to H + Br* ($^2P_{1/2}$) does exhibit substantial coherent H atom spin polarization. Figure 4.8 shows the result of monitoring the spin polarization as given by equation 4.3 with the Lyman-α laser frequency set midway between the $2p_{1/2}$ and $2p_{3/2}$ transitions, then scanning the tagging laser over the the full $n = 2 \rightarrow n = 20$ transition. This apparent change of sign of the spin polarization is clearly observed.

4.5 The Doppler Effect in SPH-RTOF

In most photodissociation experiments involving imaging, the Doppler effect is addressed experimentally by scanning the probe laser across the Doppler profile [66]. For detection of the coherent anisotropy parameters, the full velocity dependence can be obtained because they are maximal perpendicular to the laser propagation direction and they can be measured directly at the line center. Selection of a given fine-structure component is ensured through use of a narrow slit placed on the detector along the axis of the molecular beam. This results in a detection acceptance angle of 2^o, implying a Doppler selection of 0.08 cm^{-1} at the ionization threshold for a typical H atom traversing at 5 km/s. The Rydberg tagging detector design is included in the experimental apparatus section (Chapter 5) here.

This two-color excitation scheme allows us to select a single fine structure component even within a much larger Doppler envelope owing to the distinct Doppler shifts associated with the $1s \rightarrow 2p$ and $2p \rightarrow 20d$ transitions. For recoil along Z at 20 km/s, the 2p fine structure splitting corresponds to 1250 m/s at Lyman-α but 4100 m/s on the taggng transition, readily allowing isolation of only one component. Scanning both VUV and tagging lasers will allow us to record the full velocity distribution for the incoherent orientation, but we have not yet implemented the means to do this. However, we demonstrate the imaging approach by placing the Lyman-α wavelength at the very edge of the velocity distribution corresponding to the H+Br channel in HBr photodissociation, avoiding the contribution from the H+Br* channel.

Figure 4.9 below shows a velocity-mapped image of the ground state H atoms

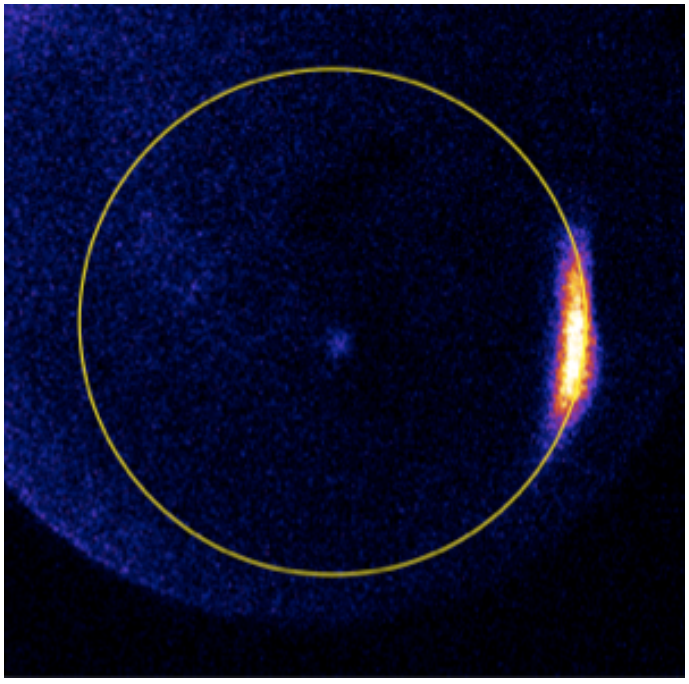

FIGURE 4.9: SPH-RTOF Velocity-mapped ion image of H atoms born from ground-state Br atoms in the photodissociation of HBr.

produced in the UV photodissociation of HBr with the above-described doppler-shifted approach. The dynamical interpretation of this image is included in Chapter 6 of this work.

CHAPTER 5

EXPERIMENTAL APPARATUS

5.1 SPH-RTOF Vacuum Chamber

A new apparatus was constructed to carry out the experiments described in this work, and a detailed description of it is therefore given here.

The SPH-RTOF apparatus (Figure 5.1) consists of two separate differentially pumped stainless steel chambers. Each chamber is pumped by its own Osaka magnetic bearing turbomolecular pump. A Proch-Trickl [67] piezoelectric valve operating at 10 Hz is mounted in the source chamber and has a nominal pulse width of 160 microseconds and a backing pressure of approximately 1200 torr. Background pressures with the molecular beam on are 2×10^{-6} torr and 6×10^{-7} torr for the source and reaction chambers, respectively. The two regions are joined by a 1/4" thick 8.0" outer diameter stainless steel plate with a skimmer mounted to it. The skimmer has a 0.5 mm orifice and resides 3 cm dounstream from the nozzle of the piezo valve. The reaction chamber is a Kimball Physics UHV 8.0" spherical octagon, measuring 6.65" inner diameter and 2" in length, with two 8" conflat ports and eight 2.75" conflat ports as shown in Figure 5.1. Ion optics are mounted in the reaction chamber via the same plate that serves as a mount for the skimmer. This arrangement, which we later describe in detail, includes a repeller, extractor, and ground electrodes. The molecular beam intersects the lasers in the interaction region which resides 5 cm from the skimmer. At this point in the supersonic expansion, the molecular beam has a diameter of 2 mm. The 2.75" CF

ports in the spherical octagon allow for a diverse arrangement in this apparatus. At the very top of the chamber resides the TOF tube used in Rydberg tagging experiments. The overall flight length is 28 cm, and consists of a stainless steel conical reducer which couples the 6" CF mount of the MCP detector to the 2.75" CF component of the spherical octagon. Perpendicular to the TOF detector are two entry windows; the VUV cell, which is later described in detail, interfaces with the reaction chamber via a bi-convex MgF_2 lens which separates the cell from the rest of the apparatus. The rydberg tagging and photolysis beams enter the chamber through a fused silica window opposite to the VUV cell. The bottom port of the apparatus serves to accomodate an aperture which makes precise spatial alignment straightforward; here, a 1/4" outer diameter stainless steel tube with 1/16" holes passes counter-propagating beams at the same point in the interaction region. The remaining 4 ports include a 2 3/4" CF flange with SHV feedthroughs for the repeller and extractor electrodes of the ion optics, as well as two additional fused silica entry windows which allows for some flexibility in experimental geometry. The final port houses an ion gauge. We find that, in addition to reporting the chamber pressure, the ionization gauge dissociates background H_2 to give H atoms that are a convenient means of verifying the production of VUV, as well as optimizing its intensity. As this instrument is equipped to do both multiphoton ionization/imaging and Rydberg TOF experiments, we detect these "ion gauge H atoms" following $1+1'$ VUV ionization with the imaging detector which terminates a second 38 cm TOF region along the molecular beam propagation axis. Details are included in Section IV below.

The tripling cell for production of the vacuum ultraviolet (VUV) light employed

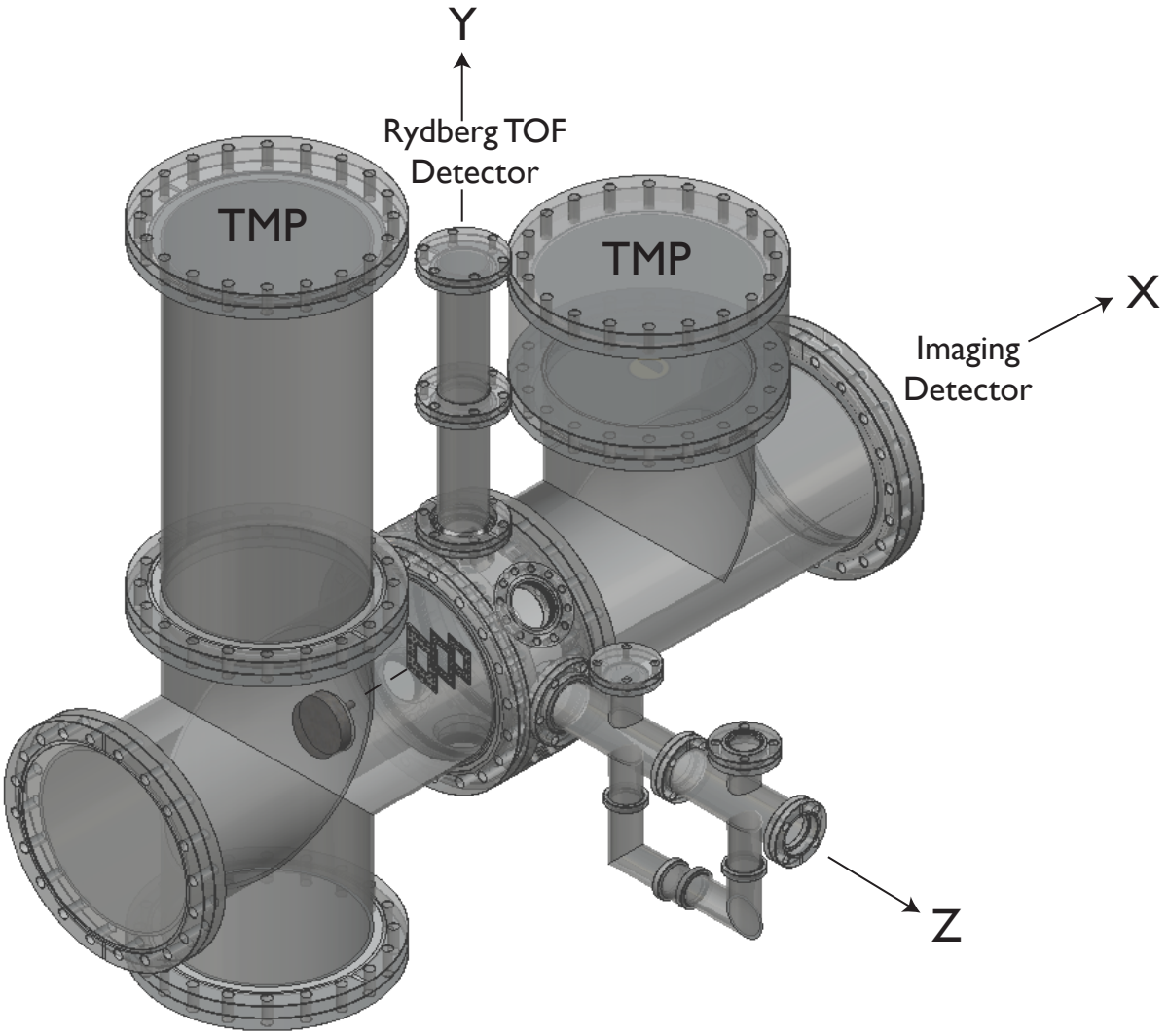

FIGURE 5.1: SPH-RTOF apparatus.

here consists of two standard conflat 2 3/4" four-way reducing crosses and two 2 1/8" elbows. This design allows for the lower half of the cell to be cooled. The temperature differential effectively circulates the Kr within, which prolong its lifetime over the course of an experiment. The cell is evacuated by a small roughing pump, and a gate valve in addition to a liquid nitrogen cooling trap is placed in between this pump and the VUV cell to prevent contamination. An MKS 500 torr Baratron Capacitance Manometer is also mounted on the VUV cell. Careful consideration was given to the choice of lenses in this design so as to prevent saturation of the H atom on the Lyman-α transition and ensure an accurate measurement of

the ground-state H atom spin-polarization. The VUV cell, while directly mounted to the reaction chamber, is separated by a 25.4 mm bi-convex MgF_2 lens (ISP Optics) with a focal length of 2.5 cm at 121.6 nm. The lens itself is held in an MDC cajon mount, and ultimately resides in the reaction chamber 7.5 cm away from the interaction region. The final distance between the MgF_2 lens and the fused silica entry window into the cell is 32 cm. In this setup, a plano-convex fused silica lens which is mounted on a translation stage 36 cm upstream from the MgF_2 lens, outside of the cell, is employed. Although the refractive indices of the 121.6 and 366 nm radiation are not sufficiently different in MgF_2 to separate the two beams at the interaction region, this arrangement implies a back focal length of 7 cm for the 121 nm radiation, while the 366 nm beam is focused well beyond this at 21.5 cm so as to minimize $1 + 1'$ ionization from Lyman-α and the 366 nm fundamental. The use of an imaging detector as described in Section IV is a convenient means of determinig experimental conditions yielding optimal VUV with minimal direct ionization. While we cannot quantify the precise power of the VUV produced, we find that 20 torr of pure Kr with the focal conditions outlined above yields sufficient VUV for pumping to the H atom 2p level without inducing saturation.

The SPH-RTOF instrument described here is equipped with a simple velocity-mapped ion optics arrangement consisting of a repeller, extractor, and ground plate. They are used in both the ion-imaging and Rydberg tagging approaches, although for very different purposes.

In the imaging approach described in Section 4.3 of this work, the gound state H

atoms undergo pulsed-field ionization in the interaction region prior to entering the TOF. Great care is taken experimentally to ionize the H atoms while still selecting a single m state under zero-field conditions. In order to do so, two different DEI pulsers are utilized for both the extractor and the repeller which are pulsed from ground to +1000V and +2000 V, respectively. The pulse duration is approximately 50 ns, although the critical parameter in this case is the pulse arrival time in relation to the Rydberg tagging probe beam which selects a single state at the 2p. A number of experimental checks are performed so as to ensure zero fields are present at the time of selectivity under these pulse-field ionization conditions. This includes scanning the probe laser across the entire n = 2 transition wherein distinct populations arising from both the 1/2 and 3/2 states are detected. Modulation of the photolysis helicity in a polarization experiment will also reflect a change of sign in the difference signal with right and left circularly polarized probe beam, implying selection of a single fine structure component. After the atoms have undergone field-ionization in the interaction region, the ions pass through the final plate held at ground and enter a 33 cm flight tube with a 20 cm outer diameter. The ions travel a total distance of 38 cm from the interaction region to the detector, which consists of two 75 mm diameter MCPs coupled to a P47 phosphor screen held at +4 kV. The front plate of the MCP is held at ground while the back plate is pulsed up to + 2000 V with a commercial DEI PVX-4140 pulser. The back plate serves to gate ions of a specific time of flight, which enables detection of a specific mass or range of masses based upon the gate pulse delay and width. The image can then be recorded using a charge coupled device camera in conjunction with a computer. We also use the output of a photomultiplier tube monitored on an

oscilloscope to provide TOF information to control mass-selectivity. In the future we will fully utilize the imaging capability of this instrument with the addition of DC slicing velocity-map ion optics.

The ion optics serve a very different purpose in our Rydberg tagging experiments. The extractor and final ground plates are both held at ground potential, and the repeller is biased to only + 10 V. This field of 10 V/cm within the interaction region eliminates unwanted prompt ions without inducing any significant Stark-shifting of the H atom transitions. After the H atoms are tagged by the probe laser, they fly 281 mm from the interaction region through the TOF region to a PHOTONIS 25mm Advanced Performance TOF detector. The detector has two MCPs with 5 micrometer diameter pores for a high channel density, a 650 picosecond pulse width and 300 picosecond rise time. The front of the detector has a fine mesh grid held at ground potential 1 mm from the surface of the front plate. The front and back plates of the MCP are held at -2.4 kV and ground, respectively. The flat input surface at the detector provides uniform ion conversion and the higher aspect ratio of the MCPs provides gains in excess of 10^7. In order to increase the Doppler selectivity of our apparatus, we placed a rectangular stainless steel mask 10 mm wide on our detector parallel to the molecular beam axis. This improvement in resolution is quantitatively discussed in Section VIII. The electron cascade in each event then strikes an anode which is coupled into an Ortec Fast-Timing Preamplifier Model VT120A, giving a 1 ns rise time and 5-V output. This signal is then sent to an Ortec 9353 multichannel scaler card (minimum dwell time 0.1 ns) which records the number of counts as a function of time. For the experiments presented here, dwell times of 3-6 ns were used, and the polarization

was cycled through automatically each 16 shots during acquisition.

5.2 SPH-RTOF Optical Layout

The UV light used for photolysis is first passed through a Thorlabs alpha-BBO Glan Polarizer. The near-pure vertically polarized beam transmitted through this Glan is then sent into a MgF_2 New Focus Berek's Polarization Compensator (Model 5540) set to half-wave retardation to yield linearly polarized light 45^o from vertical. The 45^o beam is then sent through a fused silica Hinds Photoelastic Modulator (PEM)-100 which is programmed to yield the four different photolysis polarization states ($\pm$ 45^o and RCP/LCP) utilized in a single SPH-RTOF experiment to extract the two coherent orientation parameters as discussed in subsequent sections. The PEM is oriented in its upright position for linear $\pm 45^o$ and RCP/LCP light. The PEM is used to control either the probe or photlysis polarization and is also the primary clock source to which all other delays are synchronized using a BNC 555 delay generator. The 50 kHz reference signal from the PEM triggers the BNC with a 1/5000 duty cycle, yielding a 10 Hz trigger phase-synchronous to the PEM. The outgoing beam then passes through a 24.5 mm fused-silica plano-convex lens with a focal length of 18 cm placed 23 cm before the interaction region. The Rydberg tagging probe beam, on the other hand, is either right or left-circularly polarized in this approach. Again, this beam is first passed through a calcite glan polarizer which transmits vertical light exclusively, followed by a second MgF_2 New Focus Berek's Polarization Compensator Model 5540 set to quarter-wave retardation. The circularly-polarized beam then passes

through its own 24.5 mm fused-silica convex lens with a 20 cm focal length placed 25 cm before the interaction region. The photolysis and probe beams intersect the molecular beam at a 6^o angle and are loosely focused with spot sizes of 1 mm diameter at the interaction region. Finally, the Lyman-α radiation is linearly polarized in our SPH-RTOF experiments. Section III above describes the VUV cell design which includes our choice of lenses so as to yield a 1 mm 121.6 nm spot size at the interaction region. We add here that the MgF_2 lens used to separate the VUV cell and the reaction chamber is birefringent. However, we find it is much more robust than lithium fluoride, so this lens is installed with its fast axis oriented so as not to induce unwanted ellipticity in the outgoing Lyman-α beam. We identify the fast axis outside of the chamber before mounting by placing it in the beam path prior to a Rochon prism so as to achieve maximimum extinction of a given linear polarization state. Alexander and coworkers have provided a detailed description of how one can eaily determine the helicity of the beam by inputing circularly polarized light of an indeterminate sign into a fresnel romb [68]. In addition to measuring the spin polarization of H atoms, one of the many advantages of the H-RTOF/SPH-RTOF experimental geometry is the ease with which the photofragment overall angular distribution, β, can be measured. Here, only vertical and horizontal photolysis light are required. Thus, the Berek's Compensator is removed from the photolysis beam path, and the PEM is re-mounted at 45^o to yield horizontal and vertical photolysis light. Linearly polarized probe light is also required, so we simply remove the Berek's compensator and rely upon the calcite glan for a clean vertical probe beam.

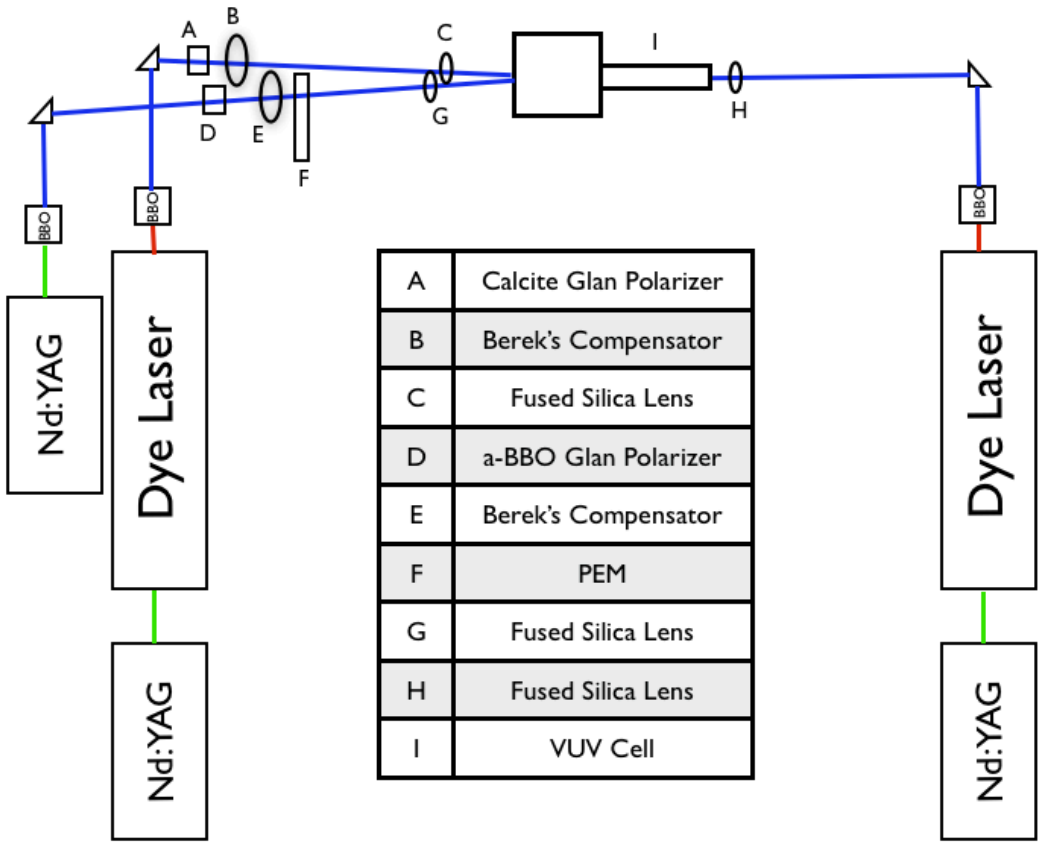

FIGURE 5.2: SPH-RTOF optical layout.

5.3 SPH-RTOF Resolution and Sensitivity Considerations

To obtain spin-sensitivity it is necessary to resolve the fine structure in the course of detection. This can be challenging because typically the Doppler envelope is many times greater than the fine structure splitting. For Rydberg tagging the velocity selection of the detector itself readily allows isolation of a single fine structure component. However, this still requires at least one of the two lasers to be narrow enough in linewidth. Generally this will be the tagging laser, which in our case is < 0.1 cm^{-1} on the doubled light. The velocity acceptance of the detector is $\delta v = vw/l$ where w is the detector width parallel to Z (determined by the mask

to be 10 mm) and l is the flight length, determined using HBr photolysis to be 281mm. This implies a frequency selection that is proportional to recoil velocity: $\delta\nu = \nu\,\delta v/c = \nu\,vw/(cl)$ with c the speed of light. For 20 km/s H atoms, this corresponds to a frequency acceptance on the tagging transition of 0.06 cm^{-1}, well below the fine structure splitting.

The UV photodissociation of thiophenol at 283 nm populates levels of the first $\pi\pi^*$ state as shown by Ashfold and coworkers [69]. Decay occurs via tunnelling to the dissociative $\pi\sigma^*$ potential energy surface. Here, no spin-polarization is expected. However, the time-of-flight spectrum for this system is shown in Figure 6A to convey a sense of the sensitivity and resolution achieved with the SPH-RTOF apparatus described here. The beam was 0.1% thiophenol in argon and the signal was averaged for one hour for the spectrum shown here. In thioppenol photodissociation, C_6H_5S fragments are formed in both their ground X^2B_1 and first excited $^2B_2$ electronic states [70]. These give rise to two broad peaks in the TOF distribution, with onsets at 22 and 28 microseconds. Discrete peaks appear within each of these, and these have been assigned by Ashfold and co-workers to excitation of specific vibrational levels in the thiophenyl radical products [69]. The TOF spectra may be converted to translational energy distributions, (P(E_T)s) through the appropriate transformations after applying the corresponding Jacobians [71]. We require $I(t)dt = I(E)dE$ so $I(E) = I(t)dt/dE$. Since $E = (1/2)mv^2$ and $v = l/t$ (with l the flight length), $dt/dE = -t^3/ml$ and $I(E) \propto t^3 I(t)$. That is, one must scale the signal intensity by the cube of the flight time before converting time to energy [72]. There is also an adjustment for the difference in center-of-mass vs. laboratory frame solid angle that adds an additional correction of v^2/u^2,

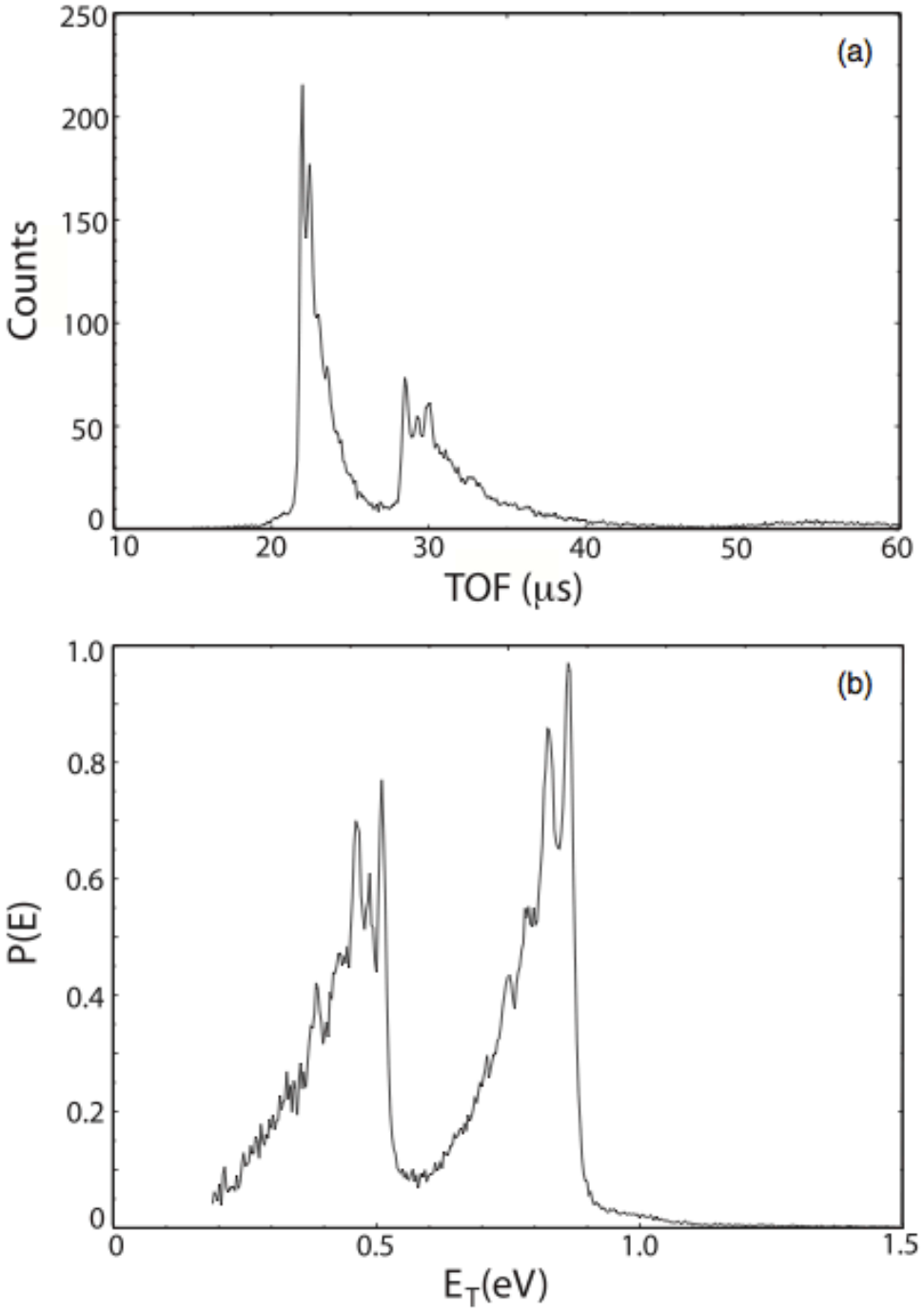

FIGURE 5.3: TOF (A) and P(E) (B) spectra for the 283 nm photodissociation of thiophenol.

where v is the laboratory frame recoil velocity and u is the center-of-mass frame recoil velocity. [71] For conditions in which the H atom velocity is very low and approaching the molecular beam veloicty this can play a role. However, because the center-of-mass and laboratory velocities of the H atom are so similar in these studies, this factor represents a very small correction and may be safely neglected. The final step in converting the H atom time-of-flight to the total translational energy release is to take the value obtained for the H atom itself and, using conservation of linear momentum, establish what the total translational energy release must be. This is simply given by $E_{total} = E_H(1 + m_H/m_{total})$.

Many factors can contribute to the velocity resolution in a photochemistry experiment. In general, it can be limited by the beam velocity spreads, by the flight length, which includes the size of the probe volume relative to the flight length (for time-of-flight) as well as angle-dependent variations in the flight length arising from the use of a planar detector, and by any perturbations in the course of detection. For H atom detection in general the first issue is rarely important, as H atoms almost always possess much higher recoil velocity than the parent molecules. The beam velocity spreads thus make a negligible contribution to the velocity resolution. This advantage is not present for heavier systems. However, if the time-of-flight direction is perpendicular to the beam direction, which is generally the case in photochemistry applications, then the longitudinal velocity spreads do not contribute in any case. The second issue, relative size of probe or detection volume and the flight length, is a key issue in photofragment translational spectroscopy. For electron bombardment detection it is usually an ionizer 1 cm long and a flight length 40 cm or less, implying a limiting velocity resolution of 2.5%. The great

advance of velocity map imaging meant that the substantial width of the probe volume relative to detector (5-10%) no longer made a contribution in imaging studies. With slice imaging, which can nearly eliminate chromatic aberration, velocity resolution of better than 0.5% has been achieved. For the HRTOF technique, the probe to flight length dimensions may be 1 mm out of 500 mm, implying a limiting velocity resolution of 0.2%. The final issue in velocity resolution is perturbations in detection. This takes two chief forms: ion recoil in photoioinization-based detection, and stray fields that may perturb the translational energy one intends to measure. Here again, the HRTOF method is unmatched. Protons are very light, so that any excess energy in an ionization-based detection would significantly blur the observed velocity measurement. In fact this is often the key factor limiting velocity resolution in multiphoton ionization-based imaging studies. In addition, any stray fields will influence the energy of ions in the course of detection. By using neutral Rydberg atoms and field ionization at threshold, the HRTOF technique overcomes all of these issues. The advantage in sensitivity for HRTOF is rather remarkable given that the acceptance of the detector is so small: fewer than 1 in 1000 of the product H atoms are detected, and one employs vacuum ultraviolet lasers with very low power. However, the $1s$ to $2p$ transition in hydrogen has an extremely large absorption cross section. Moreover, because the technique relies on field ionization many microseconds after the lasers have fired, there is essentially no background and very small signal count rates can easily yield excellent signal-to-noise. All of these advantages are similarly enjoyed by SPH-RTOF.

In the present apparatus we have compared the TOF peak widths for H atoms from HBr dissociation for 281 and 562 mm flight lengths. In the former case the

relative peak width was 0.53% full-width at half maximum, while for the latter it was 0.33%. The difference between the apothem and the radius, i.e., the flight length to the detector edge vs. to its center, contributes an uncertainty on the order of 0.09% for the shorter flight length and half this for the longer flight length in our case. If we ascribe the remainder of the measured velocity spread to the probe volume diameter, we determine the diameters to be 1.37 mm and 1.34 mm, for the short and long flight lengths, respectively. These are quite plausible values, and the good agreement clearly shows that the probe diameter is the dominant source of the uncertainty in the measured velocity.

CHAPTER 6

SPH-RTOF EXPERIMENTAL RESULTS

6.1 UV Photodissociation of H(D)Br: Introduction

The first application of SPH-RTOF to the UV photodissociation of HBr and DBr is reported here. Measurement of the overall spatial anisotropy, β, the branching fraction, Γ, and the complete characterization of the H atom spin-polarization within the laboratory frame expressed in terms of α_1, γ_1, and γ_1' is given and compared to theoretical calculations where available. The coherent spin-polarization measured in this approach arises exclusively as a result of the interference between dissociation along different potential energy curves, and therefore gives the asymptotic scattering phase shift, $\Delta\phi$. This represents a direct measurement of the phase difference of the matter waves associated with multiple pathways to dissociation, and may be obtained at a single wavelength with the SPH-RTOF technique.

Before presenting these results, a brief introduction to the UV photochemistry of H(D)Br is provided. This includes relevant potential energy curves calculated by Smolin et al. [6], previous experimental work focused on angular distributions and the spin-orbit excited branching from Ashfold and Wittig et al. [7], [73], and the earlier efforts to probe spin polarizaiotn by Rakitzis and coworkers.

Two distinct pathways are seen in the 213 nm photodissociation of H(D)Br,

Channel 1: H(D)Br + h$\nu \rightarrow H(^2\mathrm{S})$ + Br($^2\mathrm{P}_{3/2}$)

Channel 2: H(D)Br + hν $\rightarrow$ $H(^2S)$ + Br($^2P_{1/2}$)

wherein ground-state H(D) atoms are produced in conjunction with both spin-orbit ground-state Br atoms (Br($^2P_{3/2}$)) and spin-orbit excited Br* atoms (Br($^2P_{1/2}$)) [6].

The most detailed theoretical study of the electronic structure of HBr was reported by Smolin et al. [6] who calculated the full relativistic potential curves describing dissociation through channels (1) and (2) to spin-orbit gound and excited-state products. Eight adiabatic states, $X^1\Sigma_0^+$ (ground state), $A^1\Pi_1$ (two substates), $a^3\Pi_1$ (two substates), $a^3\Pi_2$ (two substates), and $a^3\Pi_0^-$, correlate with the lowest energy asymptote, while four states, $t^3\Sigma_1$ (two substates), $a^3\Pi_0^+$, and $t^3\Pi_0^-$, correlate with the excited-state asymptote [6]. These describe the complete set of adiabatic potential curves for the optically allowed transitions, and are shown in Figure (6.1) below.

Ashfold measured both the angular distributions and the spin-orbit branching fraction at many wavelengths, and combined their data with others' to characterize the entire range from 193 to 243 nm [7]. Near-limiting perpendicular anisotropy was seen for the Br channel at all wavelengths, but for the Br* channel the anisotropy parameter β was found to be strongly wavelength-dependent, varying from -1 at 193 nm to near 2 at 243 nm. The Br* branching fraction Γ also showed an interesting wavelength dependence, consistently around 15 % except in the region around 235 nm where it rose to 25 %. As this is the region where the β value for Br* changes rapidly, they argued that this "cusp" was likely a consequence of overlapping electronic excitations of different character. Rakitzis reported a slice imaging study of the angular momentum polarization of both Br and Br* at

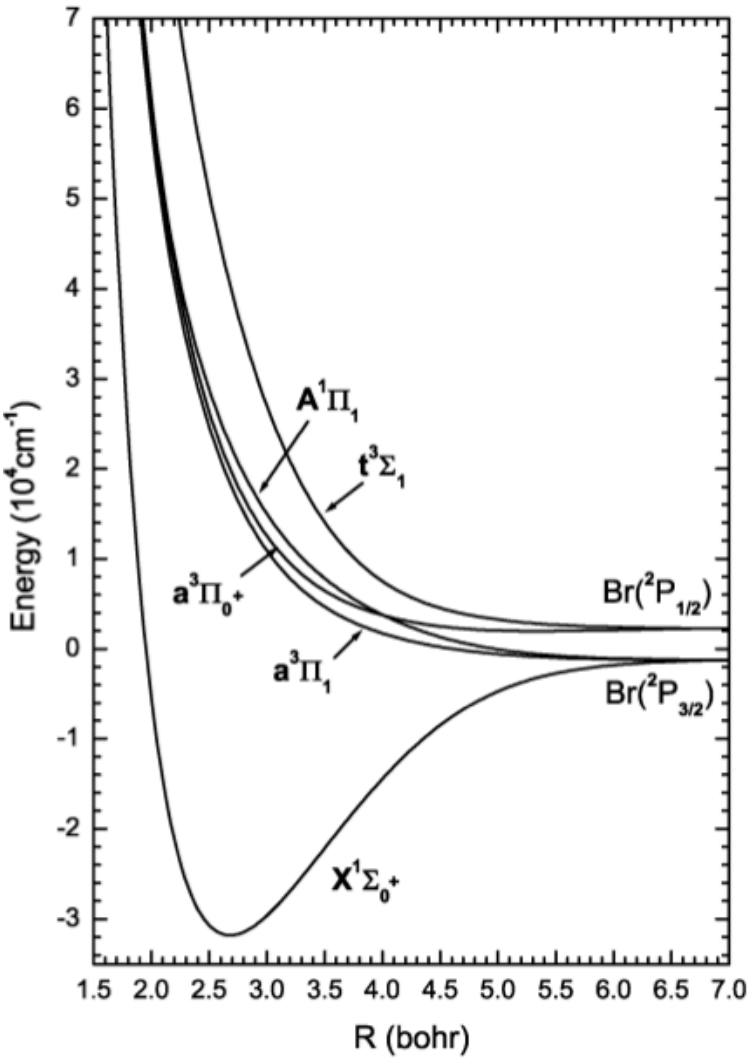

FIGURE 6.1: Adiabative potential energy surfaces by Smolin [6]).

193 nm [74], [75]. They measured β values of -0.88 for Br and -0.21 for Br*, and from the measured Br polarization they inferred the nonadiabatic branching to the $^3\Pi_1$ excited state as discussed below. They also reported the molecular-frame orientation parameters for Br and Br* produced at 193 nm by circularly polarized photolysis light, corresponding to the lab-frame α_1 and γ_1 reported here. From these they inferred near-limiting electron spin polarization for the H atom co-fragment based on conservation of angular momentum. Raktizis and coworkers subsequently reported the only direct measure of the H atom spin polarization in photodissociation [3]. This study of HBr at 193 nm was obtained via Doppler

scanning of circularly polarized Lyman-α under bulb conditions with detection of polarized fluorescence to isolate a single fine structure component in the excitation step. Because the approach relied on scanning the probe laser, the channels giving Br and Br* could not be disentangled. Values for the measured spin polarization were found to be in agreement with those inferred from the bromine atom polarization.

Using high-level ab initio methods, Smolin et al. [6] determined potential energy curves, transition moments and nonadiabatic couplings for all relevant electronic states and performed wavepacket dynamics on these curves [6]. They obtained values for the partial and total photoabsorption cross sections to the excited states as well as all possible anisotropy parameters for the Br and Br* products. They identified the dominant excitation to be via the $^3\Pi_1$ excited state which leads mainly to Br. They also identified the two states responsible for the changing Br* angular distributions: the parallel $^3\Pi_{0^+}$ state at long wavelength and perpendicular dissociation via $^3\Sigma_1$ at shorter wavelength populated via nonadiabatic transitions from the $^{1,3}\Pi_1$ states. They found the wavelength dependence of the β parameter consistent with the study of Ashfold and coworkers [7], but shifted to somewhat lower energy than seen in the experiment. They noted that these features would be very sensitive to details of the potential curves and transition moments in this threshold region. In addition, they found a shallow maximum rather than a sharp cusp in the branching fraction, and this was also shifted to lower energy. More recently, Valero et al. [12] used HBr photodissociation as a test case to examine the possibility of using constant spin-orbit coupling and a spin-coupled diabatic representation to contruct potential curves for semiclassical trajectory studies [12].

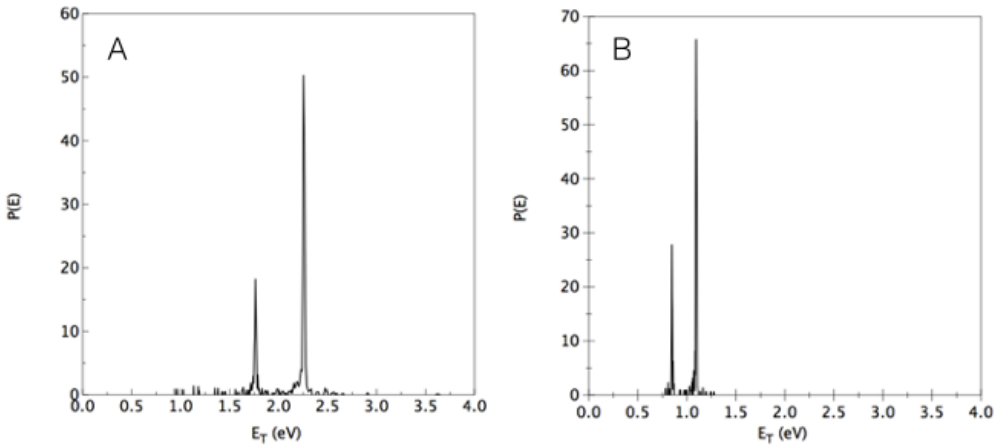

FIGURE 6.2: Translational energy distributions for A) HBr and B) DBr at 213 nm photodissociation acquired with the apparatus described in this work. The lower-energy peaks in both spectra correspond to H atoms associated with spin-orbit excited Br atoms, whereas the higher-energy peak corresponds to H atoms associated with ground-state Br atoms.

Their results reproduced much of the features of the Smolin et al. study, and they were also able to obtain the cusp in the wavelength-dependent branching similar to the experiments of Regan et al. They ascribed this to a larger $X^1\Sigma_{0^+} \rightarrow {}^3\Pi_{0^+}$ transition dipole moment obtained in their calculations.

The 213 nm photodissociation described in this work yields both H(D) atom product channels, as shown in the time-of-flight spectra in Figure (6.2). The translationally fast peak corresponds to H(D) atoms associated with ground-state Br, whereas the slower peak corresponds to H atoms born from excited-state Br*.

These two pathways were independently interrogated with the SPH-RTOF technique. Insight into the nonadiabatic contribution from the above-described states is achieved through the study of the velocity-dependent H atom spin-polarization. These results are reported below.

6.2 Experimental Results: Overall Spatial Anisotropy

In a diatomic molecule, the overall spatial anisotropy β reflects the symmetry of the electronic transition, perhaps as modulated by the lifetime of the excited state. Our results for the two different H(D)Br channels are compared with those calculated by Smolin et al at 213 nm. Dissociation of HBr to produce ground state Br atoms was found to occur via perpendicular transitions exclusively, where $\Omega = 0 \rightarrow \Omega = 1$. This implies dissociation along $A^1\Pi_1$ and $a^3\Pi_1$, and β = -1. Conversely, the β parameter for the Br* channel was found to be strongly wavelength-dependent [3], [6], [7]. At 213 nm, we found $\beta = 0.95$ in agreement with theory, implying mixed parallel and perpendicular transitions involving the states $a^3\Pi_{0^+}$ and $t^3\Sigma_1$. This result is shown in Figure (6.3) relative to the wavelength-dependence observed theoretically and in previous experimental work.

The photodissociation of DBr exhibits a different angular distribution for the D + Br* channel in this region of the UV. This system has been less extensively studied relative to HBr, but recent (unpublished) work by Smolin and coworkers is reported and compared with the results obtained in SPH-RTOF [11]. D atoms associated with ground state Br atoms are again produced exclusively via perpendicular dissociation. However, D atoms born from Br* have a β of 1.14, implying a greater parallel excitation from the ground $X\Sigma^+$ state to the excited $a^3\Pi_{0+}$ state relative to HBr. This is likely a consequence of the different zero-point energies

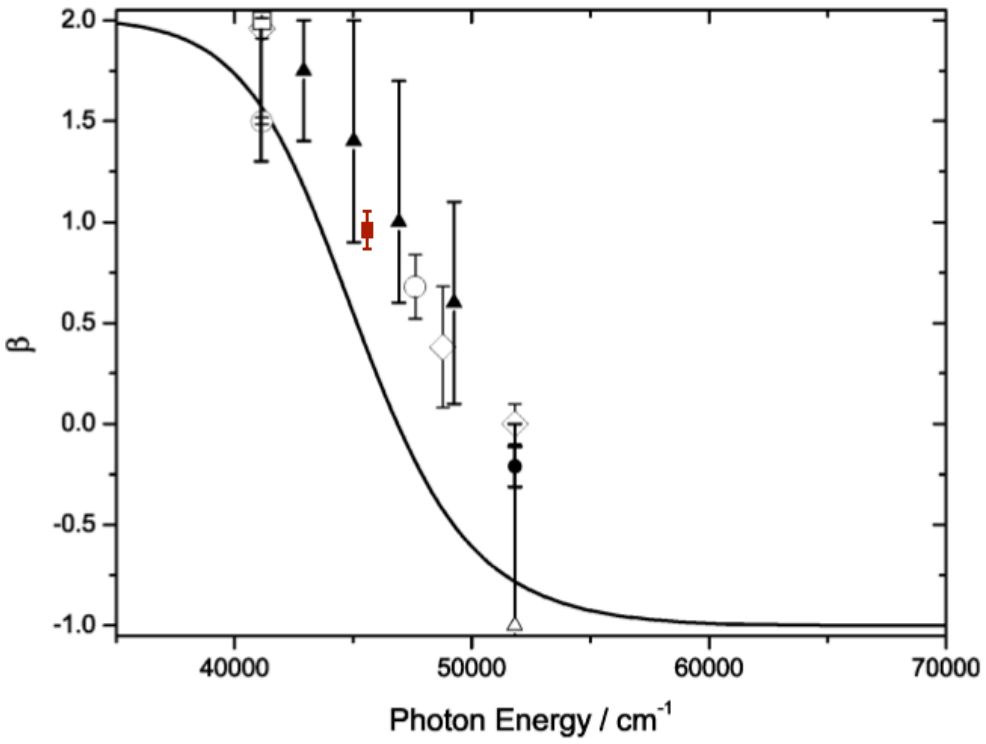

FIGURE 6.3: Wavelength dependence of the anisotropy parameter, β, adapted from Smolin et al for the H + Br* channel. The solid line represents calculations from Smolin. A number of experimental measurements also included from Ashfold Ref. [7] (filled triangle), Wittig Ref [8], (open triangles), Arikana (cite) (open squares, Rakitzis Ref [3], (filled circle), Baumfalk Ref [9] (open diamonds), Hepburn Ref [10] (open circles). This work is shown with the single solid square located at 46992.48 cm^{-1}.

and the associated Frank-Condon factors in the excitation. Smolin recently performed calculations on the UV photodissociation of DBr; although quantitatively different, his results qualitatively capture an analogous shift in β as shown in Figure (6.4) below.

This discrepancy in the parallel/perpendicular nature of the electronic excitation in H versus D revealed by β is also evident in the corresponding branching fractions and coherent spin-polarization measured in SPH-RTOF. These results are detailed in the following sections.

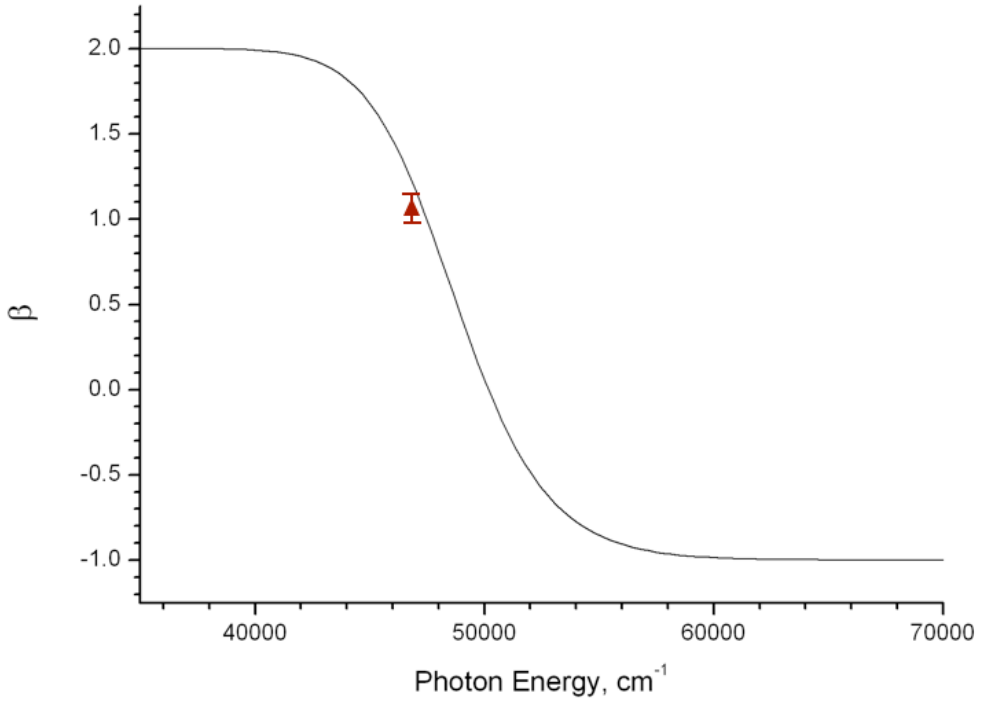

FIGURE 6.4: Wavelength dependence of the anisotropy parameter, β, adapted from Smolin et al [11] for the D + Br* channel. This work shown in red (triangle) at 46992.48 cm^{-1}.

6.3 Experimental Results: Overall Branching Fraction

A very important dynamic property for systems in which spin-orbit effects are significant is the branching fraction to the excited-state product channel [12]. This branching fraction in the case of H(D)Br photodissociation is defined as

$$\Gamma = \frac{\sigma[Br*]}{\sigma[Br] + \sigma[Br]} \tag{6.1}$$

where σ[Br] and σ[Br*] denote the partial photodissociation cross sections at a given photon wavelength to the ground and excited state of Br, respectively [12].

The exact photon energy at which the photodissociation process to produce Br* changes from parallel to perpendicular is very sensitive to the details of the electronic structure, including the potential energy curves, the couplings between them, and the transition dipole moment to a particular electronic state [76]. Previous experimental work [6] determined that the fraction of the total flux going to the Br* channel varies from 0.15 - 0.23 across a broad spectral range within the UV . HBr is unique in that the absorption intensity in the Frank-Condon region in addition to the role of nonadiabatic redistribution over the course of dissociation results in the smallest maximum branching fraction amongst all of the hydrogen halides [12].

The experimental Br* branching fractions measured in this work are 0.19 and 0.23 in H and D, respectively. Figure (6.5) below incudes the theoretical curves provided by Valero [12] in conjunction with previous experimental work for the H atom [7] [3]. Figure (6.6) includes more recent calculations by Smolin for D. We note that previous theory for the H atom by Smolin underestimated the $X^{\Sigma}{}_{0+} \rightarrow {}^{3}\Pi_{0}{}^{+}$ transition dipole moment, which may serve as an explanation for the lack of perfect agreement with the experimental D atom branching fraction reported in this work.

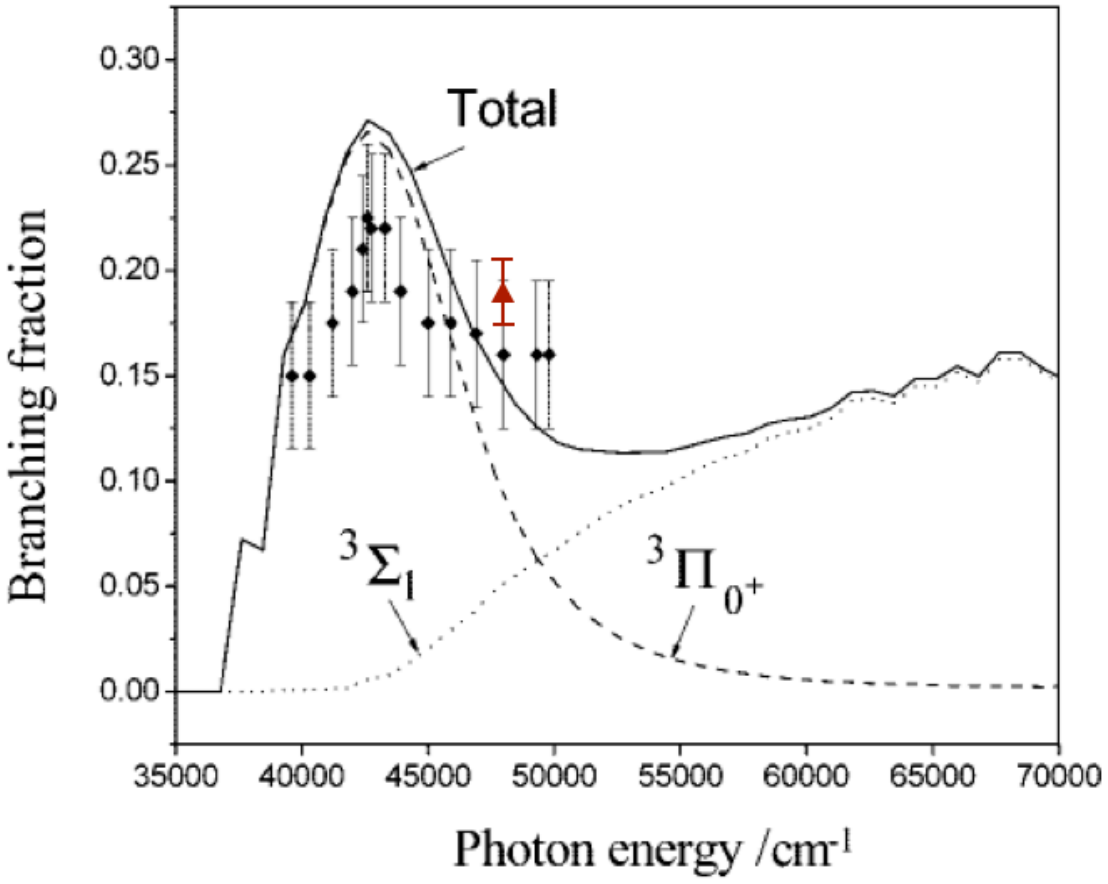

FIGURE 6.5: Branching fraction to the Br* channel adapted from Valero and coworkes [12]. The experimental measurements (cite), and the theoretical branching fraction with the contributions from the $^3\Sigma_1$ and the $^3\Pi_{0+}$ adiabatic states are shown. This work shown in red (triangle) at 46992.48 cm^{-1}.

6.4 Experimental Results: Photofragment Angular Distributions

The spin-polarization characterized by the laboratory-frame photofragment anisotropy parameters α_1, γ_1, and γ_1' is given here. We note that the final results reported account for hyperfine depolarization, which reduces the experimentally-observed degree of spin-polarization due to the spin-exchange between the electron and the nucleus [13]. This effect causes the H atom electron spin to oscillate with a period

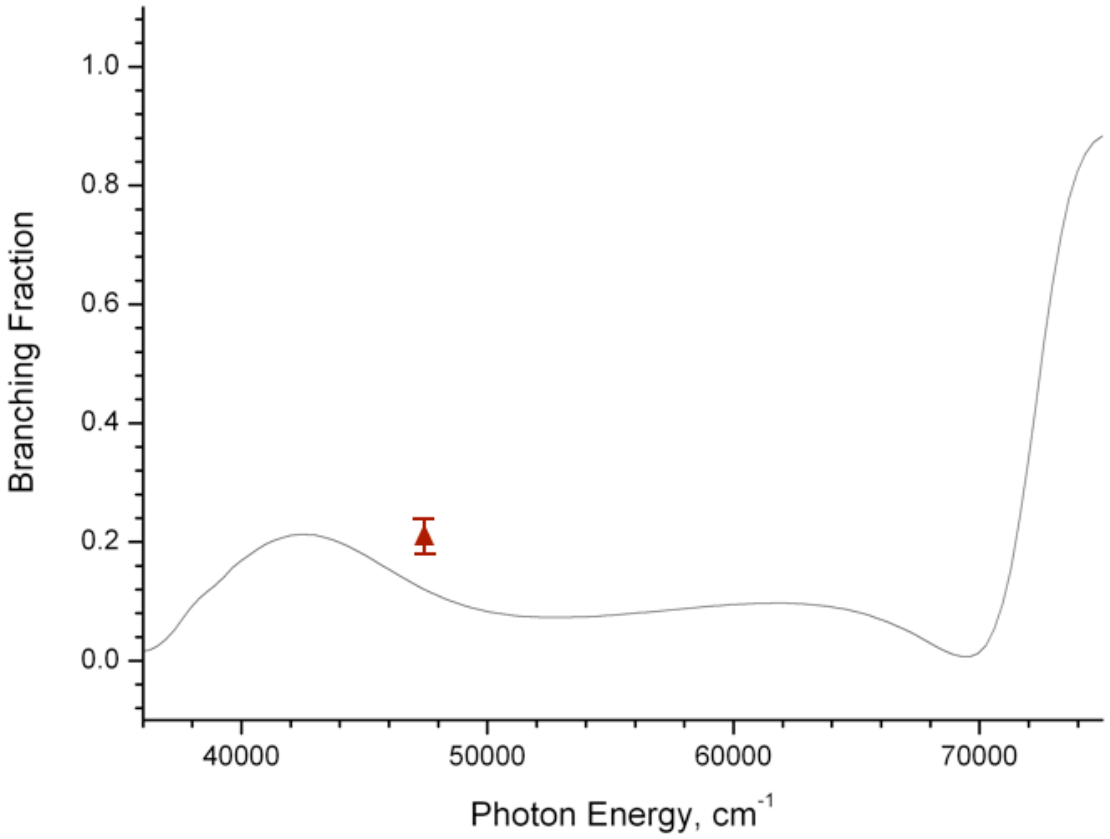

FIGURE 6.6: Wavelength dependence of the Br* branching fraction, Γ, adapted from Smolin et al [11]. This work shown in red (triangle) at 46992.48 cm^{-1}.

of 0.7 ns and results in an average reduction of the spin polarization by 0.5. Although the D atom nuclear spin is larger, its hyperfine depolarization is smaller; its timescale is 3 ns and the average reduction factor is 11/27 [13]. Both cases are taken to be in the long-time limit given our pulse durations.

6.4.1 Coherent Spin-Polarization: γ_1 and γ_1'

The coherent spin-polarization measured in SPH-RTOF is described by the laboratory-frame parameters γ_1 and γ_1', and is obtained in the Rydberg tagging TOF fashion described in Chapter 4. Both HBr and DBr were examined with this approach.

Consistent with the overall spatial anisotropy β of H(D)Br which revealed the

pure perpendicular nature of those transitions leading to H(D) atoms formed with ground-state Br products, there is no coherent spin polarization observed in this channel. Here, excitation occurs from the $X^1\Sigma^+$ state to $A^1\Pi_1$ and $a^3\Pi_1$ excited states where β = -1.

β further revealed the mixed nature of the transitions leading to H(D) atoms formed with Br*, involving parallel transitions to $a^3\Pi_{0+}$ and perpendicular transitions to $t^3\Sigma_1$ [7] [6]. This coherent excitation of multiple electronic states results in the "matter-wave" interference between them, giving rise to coherent spin-polarization characterized by γ_1 and γ_1'. This section with thus focus on the Br* channel exclusively.

The singular peaks shown in Figure 6.7 below represent the time-of-flight spectra for H(D) atoms associated with Br*. Figures 6.7(A) and 6.7(B) represent the TOF spectra acquired with right and left circularly polarized photolysis light for H and D, respectively. By integrating these peaks, correcting for the hyperfine depolarization, and invoking Equation (4 check this), we obtain the value of the measured spin polarization. For the H atom $< s_z >$ = -0.18, and for deuterium, $< s_z >$ = -0.26 for dissociation induced by circularly polarized light (Geometry I). The direction of spin in both cases is thus counter to the direction of the quantization axis, Z.

Similarly, Figures 6.7(C) and 6.7(D) illustrate the H atom spin-polarization induced by linearly polarized photolysis light (Geometry II), where $< s_z >$ = 0.19, and in D, where $< s_z >$ = 0.24. Here, the direction of spin for both systems is along the propagation direction of Z. This discrepancy between H and D in

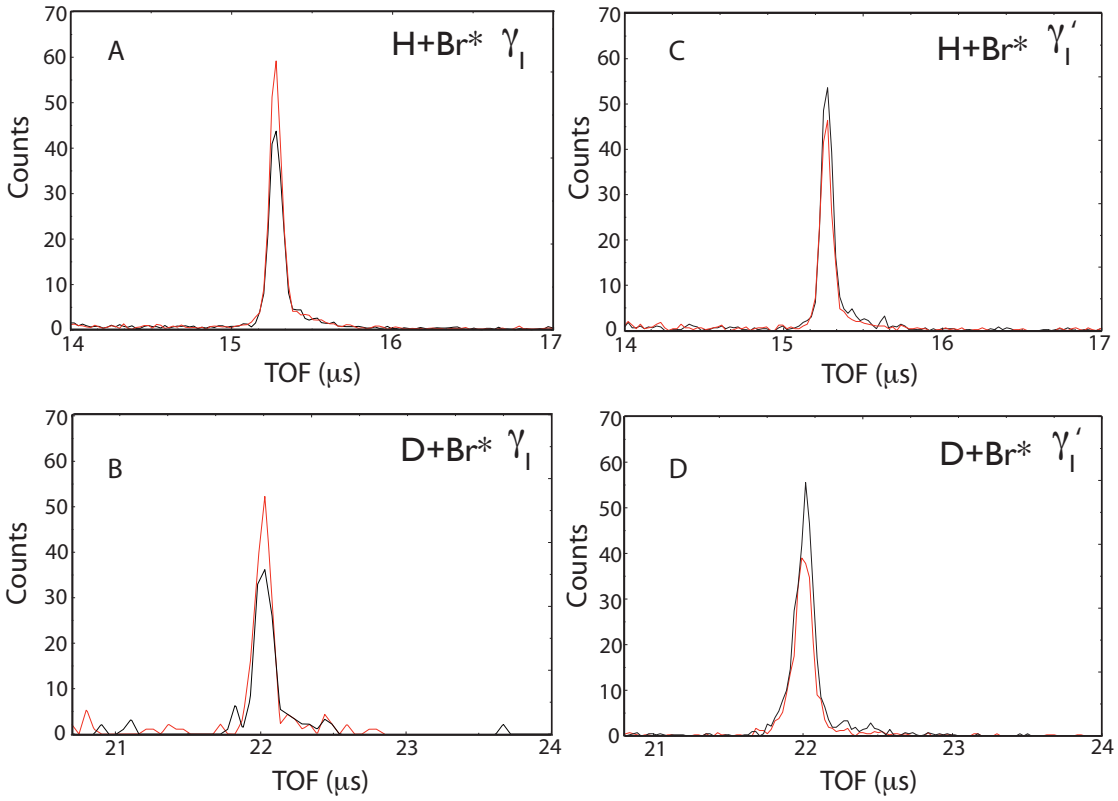

FIGURE 6.7: Spin polarization for those H(D) atoms born from Br*. A and B employ circularly polarized photolysis light to obtain the anisotropy parameter γ_1 for H and D, respectively. C and D employ linearly polarized photolysis light to obtain the anisotropy parameter γ_1' for H and D, respectively. The fast TOF Peak corresponding to H(D) atoms born from Br products are excluded as no spin-polarization is observed here.

terms of the coherent spin-polarization is consistent with the different angular distributions in this region of the UV previously provided in Section 6.2 of this work.

The coherent orientation characterized by γ_1 and γ_1' arises exclusively as a result of interference between multiple pathways to dissocation, and their ratio therefore directly provides the asymptotic scattering phase shift, $\Delta\phi$ [40]. A general illustration of this phase shift is given in Figure (**??**) below. The resulting interference pattern represents a direct measurement of the phase difference of the de Broglie wavelengths from the matter waves associated with multiple dissociation potentials, and may be obtained at a single wavelength using SPH-RTOF [38].

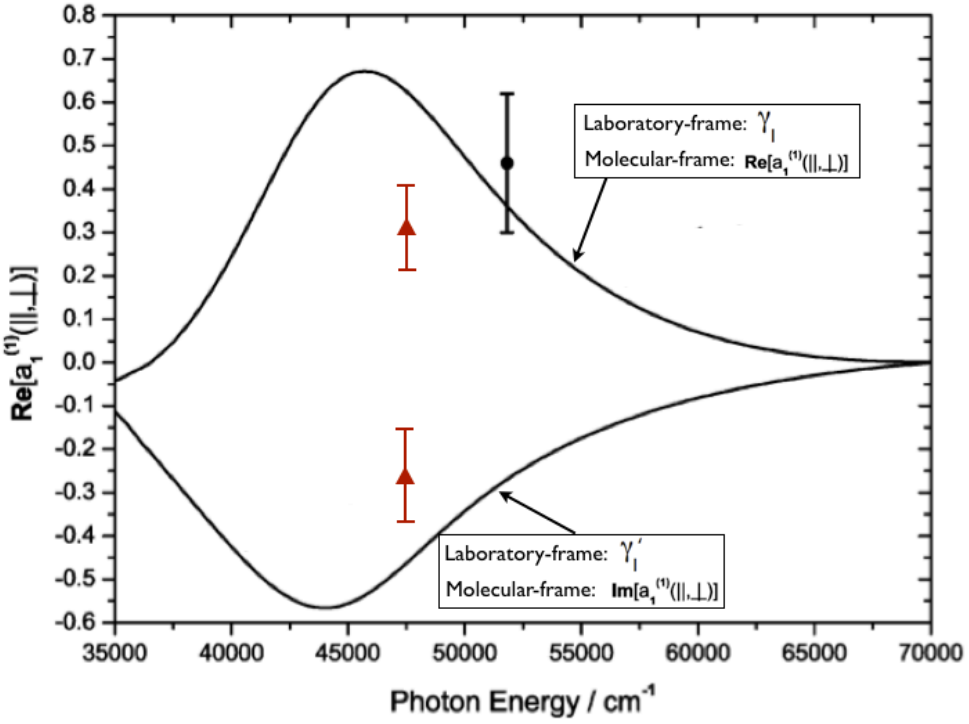

FIGURE 6.8: Wavelength dependence of the H atom coherent anisotropy parameters γ_1 and γ_1' (x and x within the molecular frame), adapted from Smolin et al. [6] for the H + Br* channel. This work shown in red (triangle) at 46992.48 cm^{-1}.

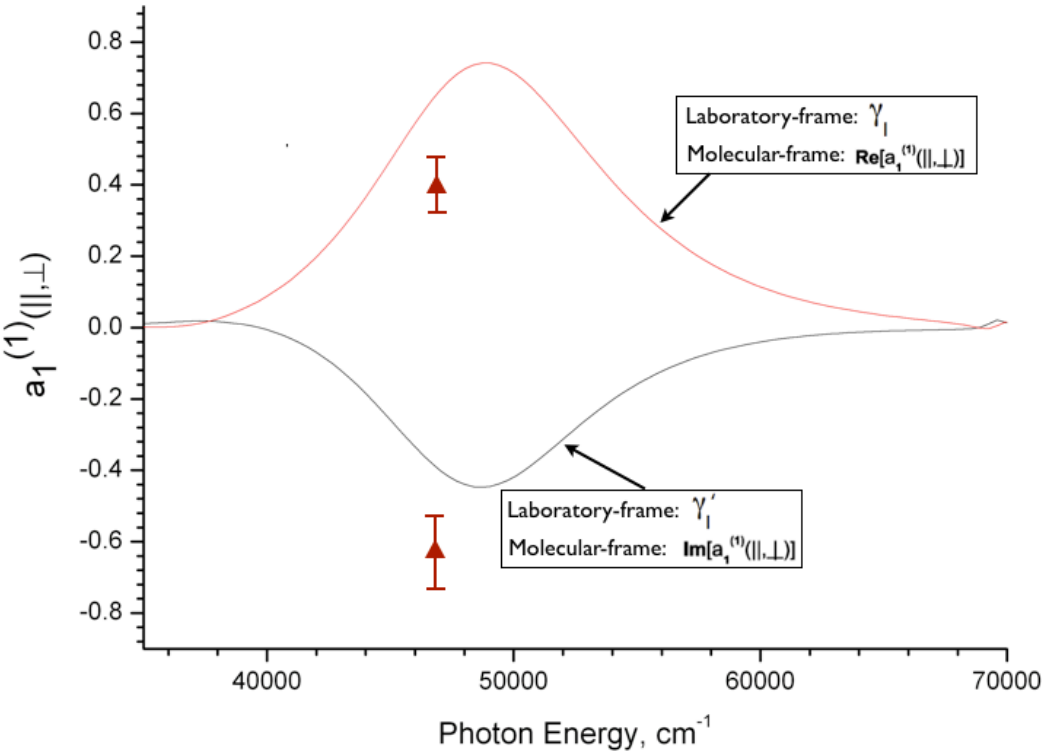

FIGURE 6.9: Wavelength dependence of the D atom coherent anisotropy parameters γ_1 and γ_1' (x and x within the molecular frame), adapted from Smolin et al. [11] for the H + Br* channel. This work shown in red (triangle) at 46992.48 cm^{-1}.

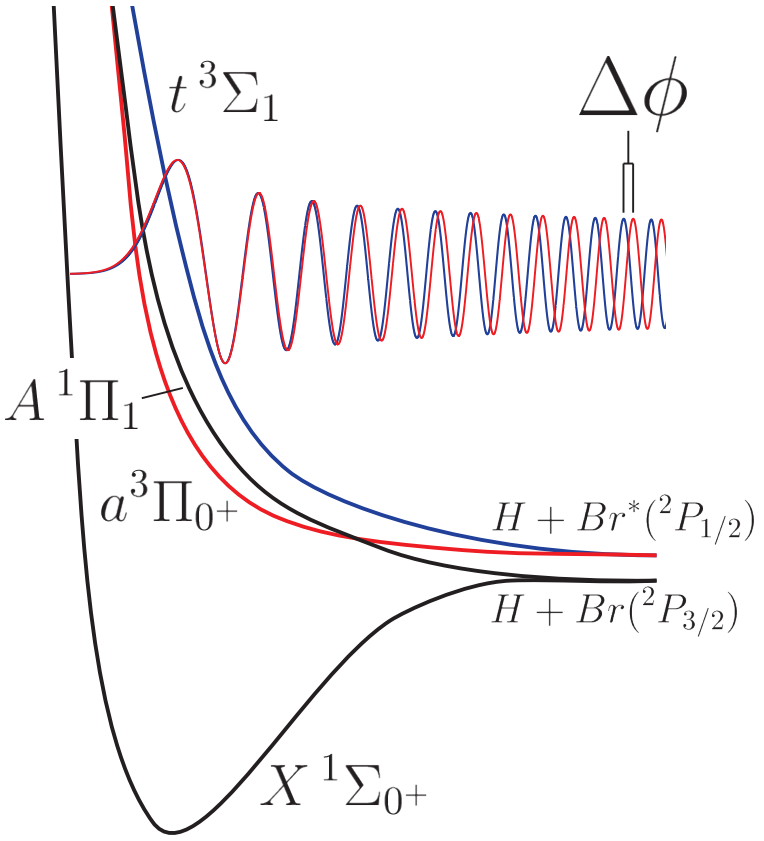

FIGURE 6.10: Potential energy curves for HBr relevant to the H(D) + Br* channel. The scattering phase shift $\Delta\,\phi$ derived from the measured H atom spin polarization is shown schematically arising from interference between dissociation along the $a^3\Pi_{0+}$ and $t^3\Sigma_1$ curves.

Equation (6.2) represents the phase shift in H(D)Br photodissociation along the $a^3\Pi_(0+$ and $t^3\Sigma_1$ potential curves:

$$\Delta\phi(a^3\Pi_{0+}, t^3\Sigma_1) \;=\; \tan^{-1}\left(\frac{\gamma_1'}{\gamma_1}\right) \tag{6.2}$$

TABLE 6.1: Summary of experimental results for anisotropy parameters and Br* branching fraction. Uncertainties in parentheses are 2σ based on twenty measurements. Phase shift in radians.

	H+Br*	D+Br*
	0.95(10)	**1.14(8)**
β	1^1	1^1
Γ	**0.19(2)**	**0.23(2)**
$\gamma_1(H(D))$	**-0.15(8)**	**-0.18(4)**
$\gamma_1'(H(D))$	**0.15(10)**	**0.30(5)**
$\Delta\phi(a^3\Pi_{0+}, t^3\Sigma_1)$	**2.36**	**2.92**

The distinct angular distributions and coherent spin-polarizations in the dissociation of HBr versus DBr further extends to their relative phase differences in the asymptotic region made apparent by SPH-RTOF. $\Delta\phi$ in the H atom products born from Br* was found to be 2.36 radians, whereas this same $\Delta\phi$ in D was found to be 2.92 radians. The increased parallel contribution in this excitation as evidenced by β again suggests greater mixing between the $a^3\Pi_1$ and $t^3\Sigma_1$ excited state potentials in D relative to H.

Table 1 summarizes the coherent orientation observed in both channels with SPH-RTOF and relative to previous experimental and theoretical work.

6.4.2 Incoherent Spin-Polarization: α_1

The α_1 parameter describes the orientation arising from incoherent perpendicular transitions, where dissociation occurs along a single surface and the general excitation is characterized by $\Omega = 0 \rightarrow \Omega = 1$. H atoms born from Br are produced in an exclusively perpendicular fashion involving transitions from the ground $X^1\Sigma_{0-}$ to the excited $A^1\Pi_1$ and $a^3\Pi$ states, with an associated β parameter of -1 as reported above.

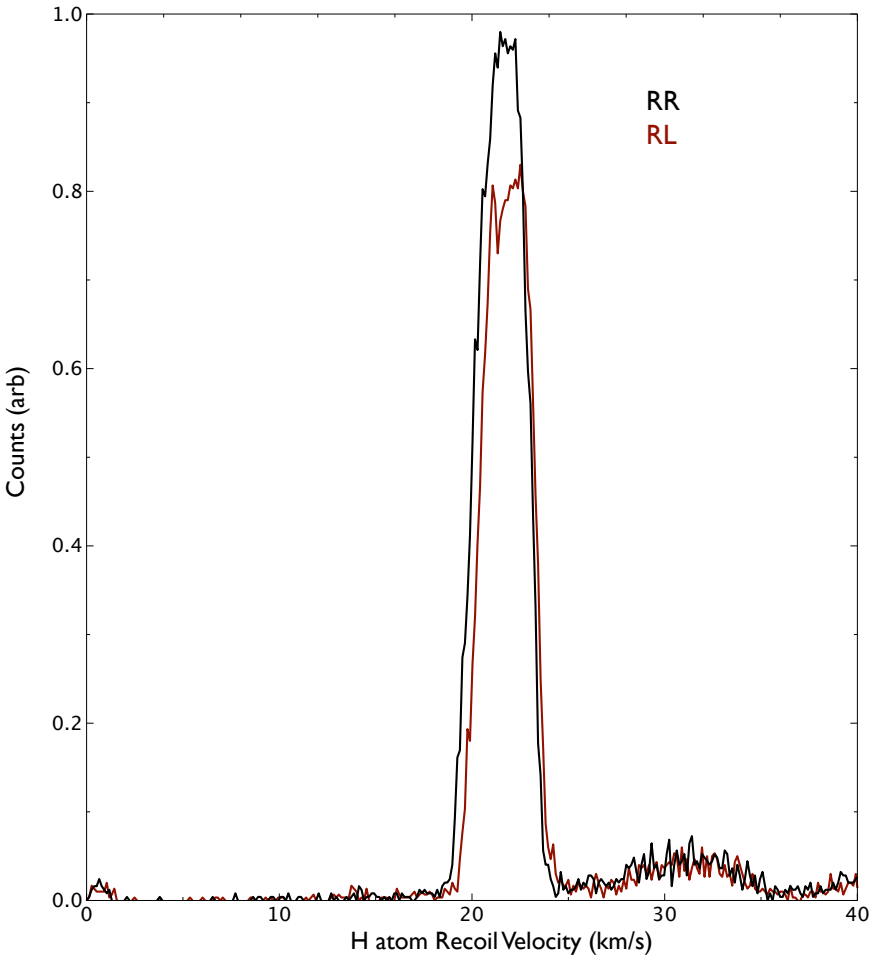

FIGURE 6.11: Recoil v of H atoms associated with Br products from right circularly-polarized photolyis light. Red and black correspond to right and left circularly-polarized probe light. The raw velocity-mapped image of this data is given in Section 4 of this work.

α_1 is obtained with the ion imaging approach described in Chapter 4, and was measured for the H + Br channel exclusively in this work. A velocity-mapped ion image of H atoms born from Br with circularly polarized photolysis light was provided in Chapter 4. The corresponding translational energy distribution is given below, where red and black represent right and left probe beam helicities, respectively. The incoherent spin polarization $< s_z >$ is obtained through integration of these peaks, correcting for the hyperfine depolarization, and invoking Equation 4.3. In this work, the H atom $< s_z > = 0.42$, where the direction of spin runs along the propagation direction of the quantization axis, Z.

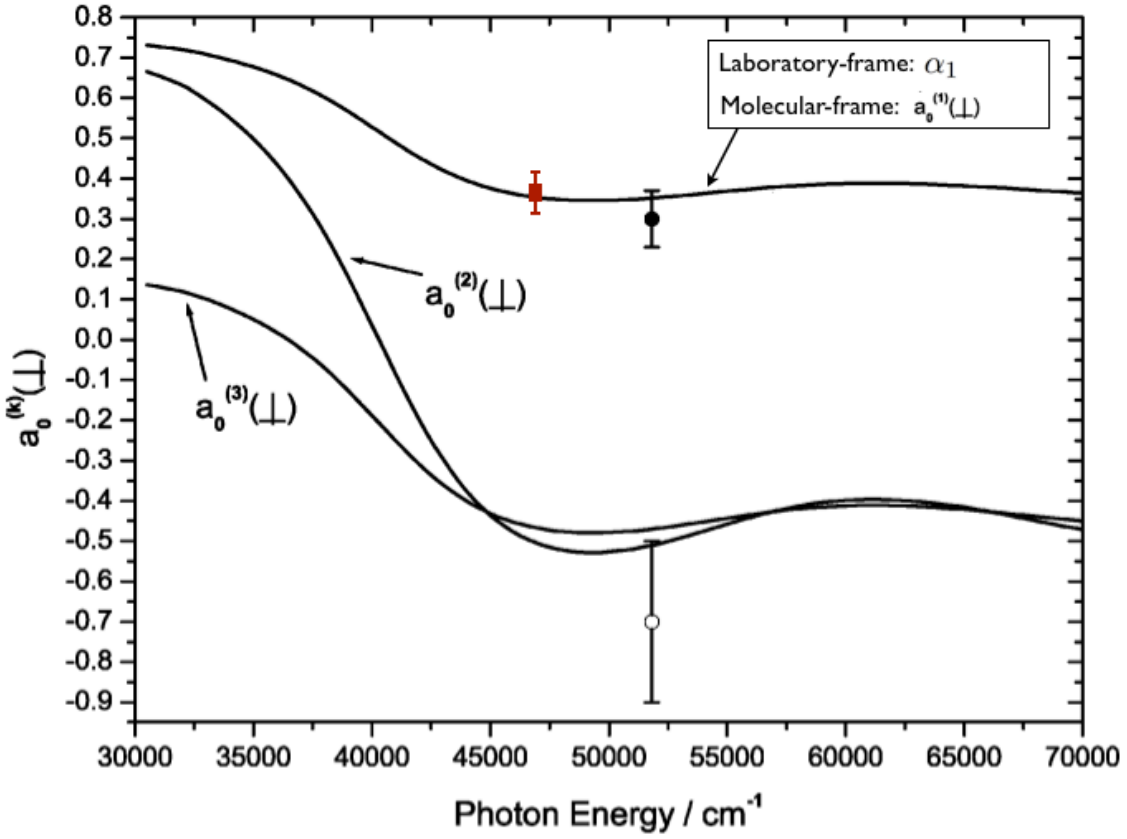

FIGURE 6.12: Incoherent anisotropy curves calculated by Smolin et al from Reference [6]. This work reported in red for the K = 1 incoherent parameter.

This result is compared with previous theoretical work from Rakitzis et al [77]. who did not directly measure the H atom, but instead measured the Br cofragment. Smolin et al. [6] also calculated the wavelength dependence of this incoherent orientation for the H atom, as shown in Figure (6.12) below. The agreement between theory and experiment in the case of inocoherent orientation measurements is very good.

In addition to the magnitude of incoherent orientation induced by circularly-polarized photolysis light, α_1 also gives the transition probability for nonadiabatic transfer between multiple electronic states [78]. The Ω components of the $A^1\Pi$ and $a^3\Pi$ states involved in the formation of H + Br products correspond asymptotically to the atomic states $|m_A, m_B\rangle$ as

$$|\pm 1\rangle_A \rightarrow \left|\mp\frac{1}{2}, \pm\frac{3}{2}\right\rangle \tag{6.3}$$

$$|\pm 1\rangle_a \rightarrow \left|\pm\frac{1}{2}, \pm\frac{1}{2}\right\rangle \tag{6.4}$$

$$|0\rangle_a \rightarrow \left|\mp\frac{1}{2}, \pm\frac{1}{2}\right\rangle \tag{6.5}$$

The nonadiabatic transition probability in the UV photodissociation of HBr is obtained from the molecular frame anistotropy parameter $a^{(1)}{}_0(\perp)$ [79], which is readily obtained from our Laboratory frame α_1.

This transition probability relates to the experimentally measured $a^{(1)}{}_0(\perp)$ in the following way:

$$a_0^{(1)}(\perp) = +\frac{(3-2p)}{\sqrt{15}} \tag{6.6}$$

where p is equal to $p_1/(1\text{-}p_2)$; p_1 and p_2 are the probabilities of nonadiabatic transfer from the $A^1\Pi_1$ to the $a^3\Pi$ and the $1^3\Sigma_1$ state, respectively [75].

Rakitzis calculated the nonadiabatic transition probability for the H + Br channel at 193 nm photodissociation [75]. Their results implied that after excitation to the primary absorber, the $A^1\Pi$ state, only 6% dissociates adiabatically (eq. 6.3), whereas 80% transfers nonadiabatically to the $a^3\Pi$ state (eq. 6.4), and 14% to the $1^3\Sigma_1$ state, both of which involve an H spin flip [75]. We too can assume a contribution of 100% from adiabatic excitation to the $A^1\Pi_1$ state based upon the -1 β value obtained for the H + Br channel, and thus obtain the same value of the nonadiabatic transition probability, in agreement with theoretical predictions from Smolin et al [6].

CHAPTER 7

CONCLUSION AND OUTLOOK

7.1 Gauge Theory in SPH

The SPH-RTOF results for H(D)Br shown here represent the first direct experimental measurement of the velocity-dependent H atom spin polarization. All three orientation anisotropy parameters, α_1, γ_1, and γ_1' are obtained as a function of recoil speed, which can be directly related to the internal state of the cofragment. As a result, it is possible to decipher the shape of the dissociated wavepacket which subsequently yields insight into the bond-breaking process. The role of spin-orbit coupling in bond fission is made particularly apparent in this approach, as it is this phenomenon that ultimately gives rise to the H atom spin-polarization observed. Finally, the quantum features of the dissociation event and role of non-adiabatic processes can be revealed through SPH-RTOF. Application to larger tri- and polyatomic systems in which coherent effects dominate the dissociation dynamics will be the central focus of future SPH-RTOF experiments. Chernyak et al. [80] have recently studied H atom spin polarization produced in the photodissociation of these larger systems from the perspective of quantum field theory. A detailed description will be given in a future publication, but a brief summary of their conclusions is presented here.

The gauge-field approach assumes zero angular momentum of the parent molecule, and employs the *wavepacket* approach to understand polyatomic dissociation [80]. According to the standard theory of photodissociation in the case of a fixed laser

frequency, all dynamical information on the process that can be retrieved at large recoil distances is contained in the matrix elements $T_{n_1n_2,E}(n) = \langle \Psi_{n_1n_2,E}(n)|\hat{\mu}|\Psi_0\rangle$ of the dipole operator $\hat{\mu}$ between the ground $|\Psi_0\rangle$ and dissociated states $|\Psi_{n_1n_2,E}(n)\rangle$.

The dissociated states are given by the eigenstates of the molecular Hamiltonian H, and can be parameterized by the value of energy and the discrete eigenstates $|n_1\rangle$ and $|n_2\rangle$ of the first and second fragments, respectively. Determination of these matrix elements $T_{n_1n_2,E}(n)$ in terms of the eigenstate picture is a difficult, if not impossible task.

The wavepacket approach provides an alternative to this method, which utilizes the fact that a dissociated state is a molecular stationary state. We can therefore recast the above in the following way [80]:

$$T_{n_1n_2,E}(n) = e^{-i\omega t}\langle|\Psi_{n_1n_2,E}(n)|\Psi(t)\rangle, \quad |\Psi(t)\rangle = e^{-i\hbar^{-1}\hat{H}}\hat{\mu}|\Psi_0\rangle, \quad \omega = \hbar^{-1}(E - E_0) \tag{7.1}$$

where ω is the resonant laser frequency, and $|\Psi(t)\rangle$ can be referred to as the dissociated wavepacket that can be calculated by solving the dynamical Schrödinger equation. When t exceeds the dissociation time, which is $\sim$ 50fs for direct dissociation in these studies, the dissociated wavepacket $|\Psi(t)\rangle$ is dominated by large recoil distances, where the interaction between the fragments can be neglected, and the dissociated eigenstates in the r.h.s. of the expression for $T_{n_1n_2,E}(n)$ [Eq. (7.1)] can be replaced by its large r asymptotic value, which is explicitly known

$$|\Psi(n,r)\rangle \sim \frac{ikr}{r}\Psi_{n_1n_2}(n)|n_1\rangle \otimes |n_2\rangle, \tag{7.2}$$

and the matrix element T can be explicitly calculated, once $|\Psi(t)\rangle$ is identified. Interpretations in terms of the wavepacket method are therefore done by understanding the dynamics of the latter.

Analysis of the molecular Hamiltonian where provides a simple explanation as to when one could expect to see spin-polarized H atoms produced in photodissociation. The molecular Hamiltonian acting on the wavepacket $\Psi(\xi) = \sum_\alpha \Psi_\alpha(\xi)|\alpha(\xi)\rangle$, where j and J are the operators of the purely electronic and total angular momenta, and ξ represents the set of $3N-6=3$ reduced nuclear coordinates, while $\alpha(\xi)$ is a set of adiabatic states and be partitioned as

$$\hat{H} = \hat{H}_{\rm s} + \hat{H}_{\rm r}, \quad \hat{H}_{\rm r} = \frac{\hbar^2}{2}\sum_{ab} I^{ab}(\xi)(\hat{J}_a\hat{J}_b + \hat{j}_a\hat{j}_b + (\hat{J}_a\hat{j}_b - \hat{j}_a\hat{J}_b)). \tag{7.3}$$

Here, $\hat{H}_s$ represents the electronic Hamiltonian and the purely vibrational component of the kinetic energy of the nuclei, and H_r is the purely rotational component. Both $\hat{H}_r$ and $\hat{H}_s$ Hamiltonians respect the rotational O(3) symmetry. However, there are two additional symmetries that are *not* preserved by the molecule Hamiltonian due to interactions between vibrations and rotations; namely, the symmetry of the electronic term, which can be A′ and A″, as well as the in-plane versus orthogonal polarization (the vector feature of $\Psi(t)$) of the wavepacket in the molecular frame. They find that $\hat{H}_s$ respects both additional symmetries, whereas $\hat{H}_r$ violates both. Due to inversion symmetry, when the ground state is at zero angular momentum and has A′ symmetry, the dissociating wavepacket $\Psi(t)$ at t=0 is either A′ with in-plane polarization, determined by the transition dipole in the molecular frame, or A″ with orthogonal polarization in the molecular frame. If

$\hat{H}_r$ is neglected, the above is also true for the dissociated wavepacket. In tri- and polyatomic photodissociation, the dominant excitations are to states of a" symmetry, which implies orthogonal polarization in the dissociated wavepacket, and zero overall spin polarization. However, Chernyak demonstrates that under sufficiently high-resolution conditions and at low-J values, it is possible to see spin-polarization, even when the primary excitations are to the orthogonal a" states. Briefly, in order to probe fragment states with different values of j, one needs to project the dissociated wavepacket onto the asymptotic states, which requires accounting for $\hat{H}_s$ [80]. As a result, the projected states acquire in-plane excitation, and thus, spin-polarization. This effect however is pronouced *only* for low-j values of the fragment angular momenta, since for high-j the contribution of $\hat{H}_r$ can still be neglected. The final proposed criteria for which spin-polarization would be produced in the photodissociation of tri- and polyatomic molecules includes TOF experiments with sufficiently high-resolution to decipher low-j channels whose projection can create a' states out of a" states, or probe only regions of the potential energy surface wherein a' states are efficiently excited [80].

We examined the UV photodissociation of H_2Se as a first triatomic system analogous to HBr, in which we hoped to see SPH production. Based upon our results obtained for the diatomic system HBr in which the Br spin-orbit splitting (3600 cm^{-1}) was sufficient to induce spin-polarization, one might also anticipate the possibility for spin-polarized H atoms to be produced with HSe, which has a similar spin-orbit splitting of 1763 cm^{-1}.

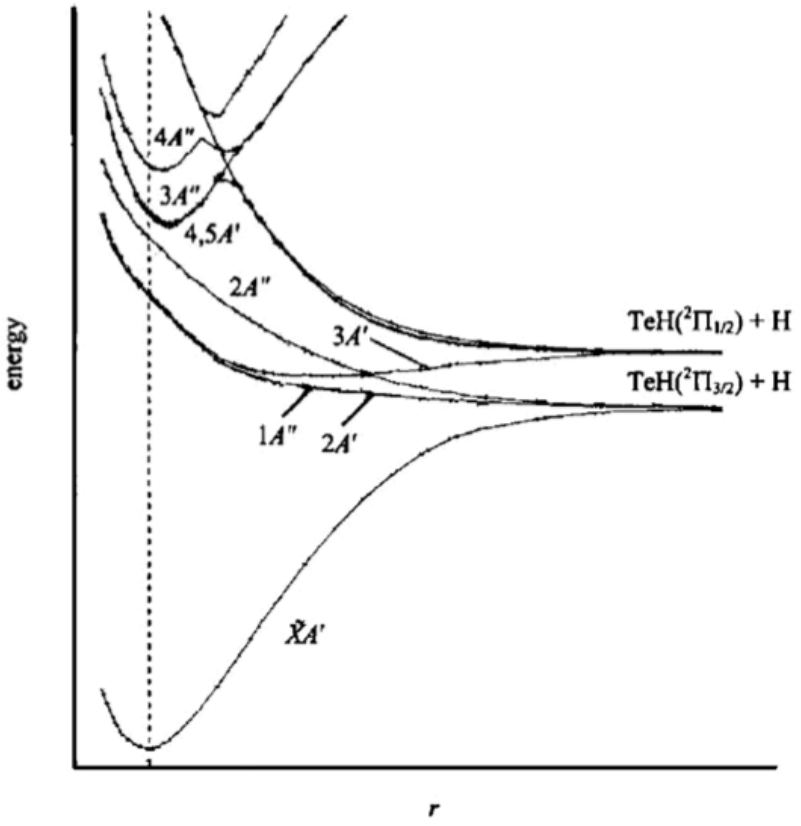

FIGURE 7.1: H_2Te potential energy surface from Ref X. The H_2Te bond angle and bond length are held at their ground state equilibrium geometry. Note that the energies for H_2Se will be different.

The photodissociation of H_2Se involves ground state H atoms associated with two different spin-orbit SeH products:

Channel 1: $H_2Se(X) + h\nu \rightarrow H(^2S) + SeH(X^2\Pi_{3/2}, \nu = 0, 1, 2, ..., N = 0, 1, 2, ...)$

Channel 2: $H_2Se(X) + h\nu \rightarrow H(^2S) + SeH(X^2\Pi_{1/2}, \nu = 0, 1, 2, ..., N = 0, 1, 2, ...)$

The potential energy surfaces for H_2Se have not been calculated, but potentials for the analogous system, H_2Te, are provided below in Figure (7.1) from Ref [81]. H atoms produced from both spin-orbit states of the HSe cofragment are shown, wherein the dominant transitions leading to both spin-orbit states have A″ symmetry [82].

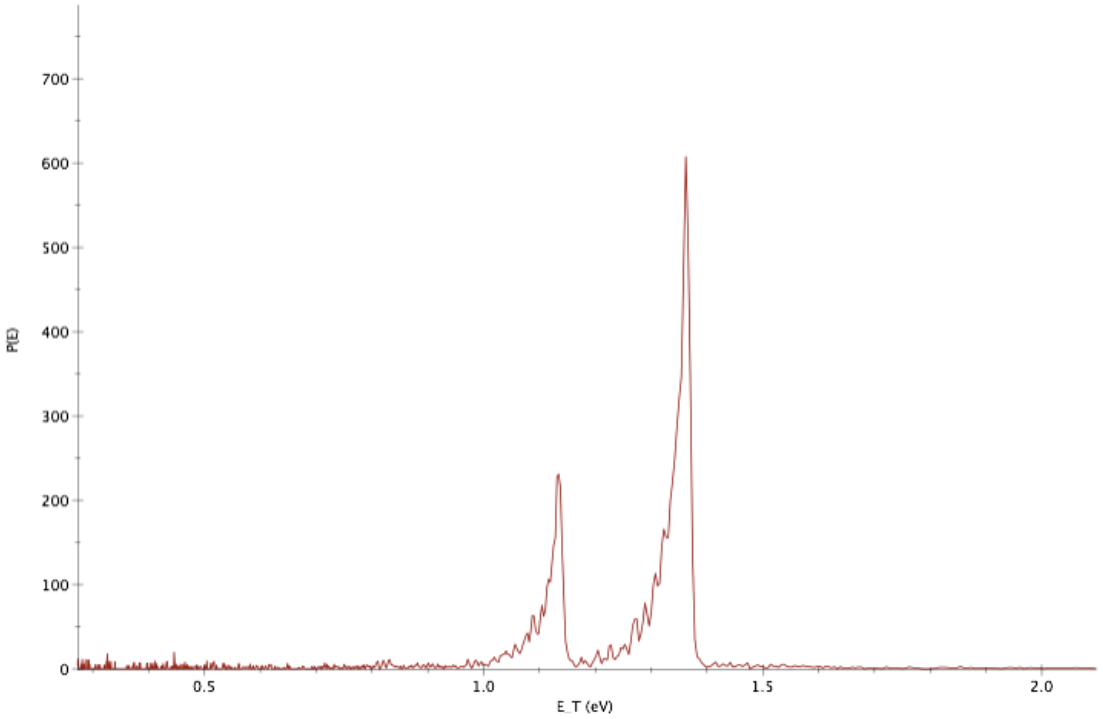

FIGURE 7.2: H_2Se translational energy distribution obtained at 213 nm photodissociation with the SPH-RTOF apparatus described in this work.

Figure (7.2) below illustrates the SPH-RTOF translational energy distribution for H atoms associated with both ground and spin-orbit excited-state HSe fragments we obtained in the photodissociation of H_2Se. Coherent spin-polarization at 213 nm was probed with both circularly and linearly polarized light. No difference is seen upon variation of the photolysis helicity, and thus a single spectrum is shown here. The results show clear rotational resolution for the HSe cofragment. Furthermore, the distribution peaks at very low rotational levels, giving some hope that we might be able to see SPH in this system even though it is an a'' excitation, given the arguments put forth above. At this point, however, the level of spin polarization is below our detectable limits, even for the low rotational levels seen here. However, higher-resolution conditions in addition to more careful analysis of the low-j states in the rich rotational structure of H_2Se will be done in future SPH-RTOF experiments.

7.2 Experimental Directions

Other systems of immediate interest to us include photofragmentation of hydrides where the role of $\pi\sigma^*$ excitations can be directly interrogated via SPH-RTOF. Specifically, phenol [83], pyrrole [84], and aniline [85]. These systems have at least one conical intersection formed between an excited state and the ground state producing H atoms and a radical in the ground or excited state [70].

Ammonia is another system in which the first excited state, a $\pi\sigma^*$ excitation, forms a conical intersection with the ground state, allowing for both adiabatic and nonadiabatic dissociation [86]. Ammonia dissociation produces different yields of ground and excited state NH_2 products depending sensitively on excitation to different predissociative bending levels in the excited state [87]. This effect arises owing to a conical intersection that funnels products to the ground state for planar geometries, but yields excited state products from direct dissociation of the excited state via nonplanar geometries [88]. Building on the extensive literature for this system, we anticipate some surprises and some insight into the method itself following high-resolution detection of SPH product.

Much recent work has been done on the photodissociation of water by Yang and others [89], [90], [91], but the spin polarization of the product H atom has not been examined. Wavelengths between 150-200 nm excite the $(^1B_1/^1A'')$ state, which correlates to ground state OH $(X^2\Pi)$ and H atoms. At shorter wavelengths, $\tilde{B}(^1B_2/^1A')$ state is excited [90]. It can form ground state OH radicals by passage through a conical intersection with the ground state at linear geometries, while water molecules in a bent geometry correlate with excited state OH $(A^2\Sigma^+)$ [91].

If there is enough energy, excited state OH ($A^2\Sigma$) is formed, while if not, the water molecule will eventually funnel down into the conical intersection and form ground state OH ($X^2\Pi$). By using the SPH-RTOF technique it may be possible to distinguish different rotational levels of OH as well as between the two electronic states of OH by the arrival time of the H atoms. We can closely examine the correlation between spin polarization of H atoms partnered with different electronic and vibrational states of OH. We can use excitation at 157 nm to probe dissociation through the $\tilde{A}^1A'$ state, and dual VUV wavelength generation as demonstrated by X. Yang for dissociation through the $\tilde{B}^1A'$ state [89].

In addition to expanding the range of systems for which to apply the SPH-RTOF approach, the future of the technique also includes the use of imaging detection exclusively to measure all three orientation parameters in distinct geometries. While Rydberg tagging is essentially a zero-background measurement, detection efficiency is vastly lower in this approach relative to ion-imaging (4π collection in imaging, versus 10^{-4} in Rydberg tagging). Recent improvements to velocity-mapped imaging have made it possible to effectively slice H atoms across a broad range of kinetic energies [92]. The modified approach utilizes a purely electrostatic ion optics design optimized for H atom slicing, in addition to a lens in the TOF drift region which allows one to obtain extraordinary high-resolution sliced images for H atom photofragments. The arrangement demonstrated a kinetic energy resolution of less than 1% percent across a range of kinetic energies [92]. This effort to implement a high-resolution imaging detection system optimized for H atoms is currently underway, which will greatly expand the versatility of the SPH-RTOF approach.

BIBLIOGRAPHY

[1] A. Beiser. Stern-gerlach experiment. *Concepts of Modern Physics*, 5th edition, 1995.

[2] T. P. Rakitzis. Pulsed-laser production and detection of spin-polarized hydrogen atoms. *ChemPhysChem*, 5:14, 2004.

[3] Dimitris Sofikitis, Luis Rubio-Lago, Lykourgos Bougas, Andrew J Alexander, and T Peter Rakitzis. Laser detection of spin-polarized hydrogen from hcl and hbr photodissociation: Comparison of h-and halogen-atom polarizations. *The Journal of Chemical Physics*, 129:144302, 2008.

[4] E. R. Wouters, M. Ahmed, D. S. Peterska, A. S. Bracker, A. G. Suits, and O. S. Vasyutinskii. Imaging the atomic orientation and alignment in photodissociation. In A. G. Suits and R. E. Continetti, editors, *Imaging in Chemical Dynamics*, page 238. American Chemical Society, Washington DC, 2000. rewiev on imaging of photofragment orbital orientation and alignment.

[5] Dave Townsend, Wen Li, Suk Kyoung Lee, Richard L Gross, and Arthur G Suits. Universal and state-resolved imaging of chemical dynamics. *The Journal of Physical Chemistry A*, 109(39):8661–8674, 2005.

[6] Andrey G Smolin, Oleg S Vasyutinskii, Gabriel G Balint-Kurti, and Alex Brown. Photodissociation of hbr. 1. electronic structure, photodissociation dynamics, and vector correlation coefficients. *The Journal of Physical Chemistry A*, 110(16):5371–5378

[7] Paul M Regan, Stephen R Langford, Andrew J Orr-Ewing, and Michael NR Ashfold. The ultraviolet photodissociation dynamics of hydrogen bromide. *The Journal of Chemical Physics*, 110:281, 1999.

[8] Z Xu, B Koplitz, and C Wittig. Determining reaction pathways and spin-orbit populations in the photodissociation of hbr and hi using velocity-aligned doppler spectroscopy. *J. Phys. Chem.*, 92(19), 1988.

[9] R Baumfalk, U Buck, C Frischkorn, SR Gandhi, and C Lauenstein. Uv photolysis of (hbr)¡ sub¿ n¡/sub¿ clusters with known size distribution. *Chemical physics letters*, 269(3):321–326, 1997.

[10] JW Hepburn, K Liu, RG Macdonald, FJ Northrup, and JC Polanyi. Dynamics of nonadiabatic reactions. i. f (2p3/2, 2p1/2)+ hbr (dbr)? hf (df)+ br (2p3/2, 2p1/2). *The Journal of Chemical Physics*, 75(7):3353–3364, 1981.

[11] A Smolin. Unpublished theoretical calculations, via email exchange. May 2014.

[12] Rosendo Valero, Donald G Truhlar, and Ahren W Jasper. Adiabatic states derived from a spin-coupled diabatic transformation: Semiclassical trajectory study of photodissociation of hbr and the construction of potential curves for libr+. *The Journal of Physical Chemistry A*, 112(25):5756–5769

[13] A.J. Orr-Ewing and R.N. Zare. Orientation and alignment of reaction products. *Annu. Rev. Phys. Chem.*, 45:315–365, 1994.

[14] N.F. Mott and H.S.W. Massey. *The Theory of Atomic Collision*. Oxford University Press, Oxford, 3rd edition edition, 1965.

[15] H. Okabe. *Photochemistry of Small Molecules.* Wiley, New York, 1978.

[16] R. Schinke. *Photodissociation Dynamics.* Cambridge University Press, Cambridge, 1993.

[17] P.L. Houston. Vector correlations in photodissociation dynamics. *J.Phys.Chem.*, 91:5388–5397, 1987. review on vect corr.

[18] G.E. Hall and P.L. Houston. Vector correlations in photodissociation dynamics. *Annu. Rev. Phys. Chem.*, 40:375–405, 1989. ?

[19] A.G. Suits, R.L. Miller, L.S. Bontuyan, and P.L. Houston. Photofragment vector correlations by ion imaging: $O_2[a^1\Delta_g(v, J)]$. *J. Chem. Soc. Faraday Trans.*, 89:1443–1447, 1993.

[20] G. G. Balint-Kurti, A.J. Orr-Ewing, J.A. Beswick, A. Brown, and O.S. Vasyutinskii. Vector correlations and alignment parameters in the photodissociation of hf and df. *J. Chem. Phys*, 116:10760, 2002. HF photodissociation, determination of anisotropy parameters.

[21] Mikhail B Krasilnikov, Vladislav V Kuznetsov, Arthur G Suits, and Oleg S Vasyutinskii. Vector correlations in photodissociation of polarized polyatomic molecules beyond the axial recoil limit. *Physical Chemistry Chemical Physics*, 13(18):8163–8174, 2011.

[22] D.A. Varshalovich, A.N. Moskalev, and V.K. Khersonskii. *Quantum Theory of Angular Momentum.* World Scientific, New York, Singapore, 1988.

[23] Arthur G Suits and Oleg S Vasyutinskii. Imaging atomic orbital polarization in photodissociation. *Chem. Rev.*, 108:3706–3746, 2008.

[24] E.B. Alexandrov M.P. Chaika, G.I. Khvostenko. *Interference of atomic states.* Springer, 1993.

[25] A.S. Bracker, E.R. Wouters, A.G. Suits, Y.T. Lee, and O.S. Vasyutinskii. Observation of coherent and incoherent dissociation mechanisms in the angular distribution of atomic photofragment alignment. *Phys. Rev. Lett.*, 80: 1626–1629, 1998.

[26] M. Ahmed, D.S. Peterka, O.S. Vasyutinskii, and A.G. Suits. Coherence in polyatomic photodissociation: aligned $O(^3P)$ from photodissociation of NO_2 at 212.8 nm. *J. Chem.Phys*, 110:4115–4118, 1999.

[27] T.P. Rakitzis, S.A. Kandel, A.J. Alexander, Z.H. Kim, and R.N. Zare. Photofragment helicity caused by matter-wave interference from multiple dissociative states. *Science*, 281:1346–1350, 1998.

[28] R.N. Zare. *Angular Momentum.* Wiley, New York, 1988.

[29] M. Auzinsh and R. Ferber. *Optical Polarization of Molecules.* Cambridge University Press, 1995.

[30] A.S. Bracker, E.R. Wouters, A.G. Suits, and O.S. Vasyutinskii. Imaging the alignment angular distribution: State symmetries, coherence effects and nonadiabatic interactions in photodissociation. *J. Chem. Phys.*, 110:6749–6765, 1999.

[31] A. Brown, G. G. Balint-Kurti, and O.S. Vasyutinskii. Photodissociation of hcl and dcl: Polarization of atomic photofragments. *JPC*, 108:7790, 2004. HCl photodissociation, determination of anisotropy parameters.

[32] T. P. Rakitzis, P. C. Samartzis, and T. N. Kitsopoulos. Complete measurement of s(^{1}d$_2$) photofragment alignment from abel-invertible ion images. *Phys. Rev. Lett.*, 87:123001, 2001.

[33] D. Townsend, S. K. Lee, and A. G. Suits. Orbital polarization from dc slice imaging: S(^{1}d$_2$) alignment in the photodissociation of ethylene sulfide. *Chem. Phys*, 301:197, 2004.

[34] Y. Mo, H. Katayanagi, M.C. Heaven, and T. Suzuki. Simultaneous measurement of recoil velocity and alignment of S(^{1}D$_2$) atoms in photodissociation of OCS. *Phys. Rev. Lett.*, 77:830, 1996.

[35] A.T.J.B. Eppink, D.H. Parker, M.H.M. Janssen, B. Buijsse, and W.J. van der Zande. Production of maximally aligned O(^{1}D) atoms from two-step photodissociation of molecular oxygen. *J. Chem.Phys.*, 108:1305–1308, 1998.

[36] M. Ahmed, D.S. Peterka, E.R. Wouters, O.S. Vasyutinskii, and A.G. Suits. Atomic orbital alignment and coherence in N_20 photodissociation at 193.3 nm. *Faraday Transactions*, 1999.

[37] Bernadette M Broderick, Yumin Lee, Michael B Doyle, Oleg S Vasyutinskii, and Arthur G Suits. Velocity distribution of hydrogen atom spin polarization. *The Journal of Physical Chemistry Letters*, 4(20):3489–3493, 2013.

[38] Bernadette M Broderick, Yumin Lee, Michael B Doyle, Vladimir Y Chernyak, Oleg S Vasyutinskii, and Arthur G Suits. Spin-polarized hydrogen rydberg time-of-flight: Experimental measurement of the velocity-dependent h atom spin-polarization. *Review of Scientific Instruments*, 85(5):053103, 2014.

[39] AP Clark, M Brouard, F Quadrini, and C Vallance. Atomic polarization in the photodissociation of diatomic molecules. *Physical Chemistry Chemical Physics*, 8(48):5591–5610, 2006.

[40] T.P. Rakitzis, S.A. Kandel, and R.N. Zare. Photolysis of ICl causes mass-dependent interference in the $Cl(^2P_{3/2})$ photofragment angular momentum distributions. *J. Chem. Phys.*, 108:8291–8294, 1998.

[41] A.G. Suits and R.E. Continetti, editors. *Imaging in Chemical Dynamics*. ACS symposium series; 770, Washington, DC, 2000.

[42] Suk Kyoung Lee. *DC Slice Ion Imaging Study of Atomic Orbital Orientation and Alignment in Photodissociation*. ProQuest, 2007.

[43] G.E. Hall, N. Sivakumar, P.L. Houston, and I. Burak. Measurement of the angular correlation between recoil velocity and angular momentum vectors in molecular photodissociation. *Phys. Rev. Lett.*, 56:1671–1674, 1986.

[44] R.N. Dixon. The determinatin of the vector correlation between photofragment rotational and translational motions from the analysis of doppler-broadened spectral line profiles. *J.Chem.Phys.*, 85:1866, 1986. bipolar harm, theory.

[45] L.D.A. Siebbeles, M. Glass-Maujean, O.S. Vasyutinskii, J.A. Beswick, and O. Roncero. Vector properties in photodissociation: Quantum treatment of the correlation between the spatial anisotropy and the angular momentum polarization of the fragments. *J.Chem.Phys.*, 100:3610, 1994. dissociation dynamics.

[46] Bretislav Friedrich and Dudley Herschbach. Stern and gerlach: How a bad cigar helped reorient atomic physics. *Physics Today*, 56(12):53–59, 2003.

[47] JD Fan and Yuriy M Malozovsky. Pauli exclusion principle. *International Journal of Modern Physics B*, 27(15), 2013.

[48] Paul Adrien Maurice Dirac. A new notation for quantum mechanics. In *Mathematical Proceedings of the Cambridge Philosophical Society*, volume 35, pages 416–418. Cambridge Univ Press, 1939.

[49] JTM Walraven. Trapping and cooling of (anti) hydrogen. *Hyperfine Interactions*, 76(1):203–220, 1993.

[50] H-G Gaul and E Steffens. A highly sensitive breit-rabi type polarimeter for an internal polarized hydrogen and deuterium target. *Nuclear Instruments and Methods in Physics Research Section A: Accelerators, Spectrometers, Detectors and Associated Equipment*, 316(2):297–305, 1992.

[51] O.S. Vasyutinskii. Orientation of atoms during photodissociation of molecules. *Sov. Phys. JETP Lett.*, 31:428, 1980.

[52] O.S. Vasyutinskii. Contribution to the theory of the effect of orientation of atoms produced in photodissociation of molecules. *Sov. Phys. JETP*, 54: 855–861, 1981.

[53] T. P. Rakitzis, P. C. Samartzis, R. L. Toomes, T. N. Kitsopoulos, A. Brown, G. G. Balint-Kurti, O. S. Vasyutinskii, and J. A. Beswick. Spin-polarized hydrogen atoms from molecular photodissociation. *Science*, 300:1936, 2003.

[54] B.V. Picheyev, A.G. Smolin, and O.S. Vasyutinskii. Ground state polarized photofragments study by using resonance and off-resonance probe beam techniques. *J. Phys. Chem.*, 101:7614–7626, 1997.

[55] K. Blum. *Density Matrix Theory and Applications*. Plenum, New York, 2 edition, 1996.

[56] W. Happer. *Rev. Mod. Phys.*, 44:170, 1972. review on optical pumping.

[57] H Joachim Krautwald, Ludger Schnieder, Karl H Welge, and Michael NR Ashfold. Hydrogen-atom photofragment spectroscopy. photodissociation dynamics of h2o in the b–x absorption band. *Faraday Discuss. Chem. Soc.*, 82: 99–110 0301–7249, 1986.

[58] XF Yang, DW Hwang, JJ Lin, and X Ying. Dissociation dynamics of the water molecule on the ã b electronic surface. *The Journal of Chemical Physics*, 113: 10597, 2000.

[59] R Hilbig and R Wallenstein. Enhanced production of tunable vuv radiation by phase-matched frequency tripling in krypton and xenon. *Quantum Electronics, IEEE Journal of*, 17(8):1566–1573, 1981.

[60] JP Marangos, N Shen, H Ma, MHR Hutchinson, and JP Connerade. Broadly tunable vacuum-ultraviolet radiation source employing resonant enhanced sumifference frequency mixing in krypton. *JOSA B*, 7(7):1254–1263, 1990.

[61] D.W. Chandler and P.L. Houston. Two-dimensional imaging of state-selected photodissociation process detected by multiphoton ionization. *J.Chem.Phys.*, 87:1445, 1987.

[62] A.G. Suits, R.L. Miller, L.S. Bontuyan, and P.L. Houston. *J.Chem.Soc.Faraday Trans.*, 89:1443, 1993. ion imag -.

[63] A.T.J.B. Eppink and D.H. Parker. Velocity map imaging of ions and electrons using electrostatic lenses: Application in photoelectron and photofragment ion imaging of molecular oxygen. *Rev. Sci. Instr.*, 68:3477, 1997.

[64] D.H. Parker and A.T.J.B. Eppink. Photoelectron and photofragment velocity map imaging of state-selected molecular oxygen dissociation/ionization dynamics. *J. Chem. Phys.*, 107:2357–2362, 1997.

[65] M. Minitti and A. G. Suits. *Rev. Sci. Instrum.*, 74:2530, 2003.

[66] T. Kinugawa and T. Arikawa. *J.Phys.Chem.*, 96:4801, 1992. 3-dimentional combination of ion imaging and Doppler spectroscopy.

[67] D Proch and T Trickl. A high-intensity multi-purpose piezoelectric pulsed molecular beam source. *Review of Scientific Instruments*, 60(4):713–716, 1989.

[68] Andrew J Alexander. Determination of the helicity of oriented photofragments. *The Journal of Chemical Physics*, 123:194312, 2005.

[69] Michael NR Ashfold, Adam L Devine, Richard N Dixon, Graeme A King, Michael GD Nix, and Thomas AA Oliver. Exploring nuclear motion through conical intersections in the uv photodissociation of phenols and thiophenol. *Proceedings of the National Academy of Sciences*, 105(35):12701–12706, 2008.

[70] Adam L Devine, Michael GD Nix, Richard N Dixon, and Michael NR Ashfold. Near-ultraviolet photodissociation of thiophenol. *The Journal of Physical Chemistry A*, 112(39):9563–9574, 2008.

[71] TT Warnock and RB Bernstein. Transformation relationships from center-of-mass cross section and excitation functions to observable angular and velocity distributions of scattered flux. *The Journal of Chemical Physics*, 49(4):1878–1886, 1968.

[72] Jingsong Zhang, Michael Dulligan, and Curt Wittig. Hnco+ h. nu.(193.3 nm). fwdarw. h+ nco: Center-of-mass translational energy distribution, reaction dynamics, and d0 (h-nco). *The Journal of Physical Chemistry*, 99(19):7446–7452, 1995.

[73] Z Xu, B Koplitz, and C Wittig. Kinetic and internal energy distributions via velocityaligned doppler spectroscopy: The 193 nm photodissociation of hs and hbr. *The Journal of Chemical Physics*, 87:1062, 1987.

[74] T.P. Rakitzis, P.C. Samartzis, R.L. Toomes, L. Tsigaridas, M. Coriou, D. Chestakov, A.T.J.B. Eppink, D.H. Parker, and T.N. Kitsopoulos. Photofragment alignment from the photodissociation of hcl and hbr. *Chem. Phys. Lett.*, 364:115, 2002.

[75] T. P. Rakitzis, P. C. Samartzis, R. L. Toomes, and T. N. Kitsopoulos. Measurement of br photofragment orientation and alignment from hbr photodissociation: Production of highly spin-polarized hydrogen atoms. *J. Chem. Phys.*, 121:7222, 2004.

[76] A. G. Smolin, O. S. Vasyutinskii, E. R. Wouters, and A. G. Suits. *J. Chem. Phys.*, 121:1, 2004.

[77] T. P. Rakitzis and T. N. Kitsopoulos. Measurement of cl and br photofragment alignment using slice imaging. *J. Chem. Phys.*, 116:9228, 2002.

[78] Lykourgos Bougas, Dimitris Sofikitis, Michael A Everest, Andrew J Alexander, and T Peter Rakitzis. (2+ 1) laser-induced fluorescence of spin-polarized hydrogen atoms. *The Journal of chemical physics*, 133(17):174308, 2010.

[79] T.P. Rakitzis, G.E. Hall, M.L. Costen, and R.N. Zare. Relationship between bipolar moments and molecular-frame polarization parameters in Doppler photofragment spectroscopy. *J. Chem. Phys.*, 111:8751–8754, 1999.

[80] A. Suits and V. Chernyak. Discussion on sph sensitivity. 2013.

[81] Xiaodong Zhang, Michael Johnson, and Brent Koplitz. Using anisotropy measurements from a-band photodissociation to interrogate the excited states of h2se. *The Journal of Physical Chemistry A*, 117(46):11963–11969, 2013.

[82] Xiaodong Zhang, Michael Johnson, K Thomas Lorenz, Kenneth A Cowen, and Brent Koplitz. Combining time-of-flight methods and velocity-aligned doppler spectroscopy to measure wavelength-dependent product state distributions in h2se photolysis. *The Journal of Physical Chemistry A*, 104(45): 10511–10516, 2000.

[83] Michael GD Nix, Adam L Devine, Bríd Cronin, Richard N Dixon, and Michael NR Ashfold. High resolution photofragment translational spectroscopy studies of the near ultraviolet photolysis of phenol. *The Journal of chemical physics*, 125(13):133318, 2006.

[84] Bríd Cronin, Michael GD Nix, Rafay H Qadiri, and Michael NR Ashfold. High resolution photofragment translational spectroscopy studies of the near ultraviolet photolysis of pyrrole. *Physical Chemistry Chemical Physics*, 6(21): 5031–5041, 2004.

[85] Graeme A King, Thomas AA Oliver, and Michael NR Ashfold. Dynamical insights into $\pi 1\sigma?$ state mediated photodissociation of aniline. *The Journal of chemical physics*, 132(21):214307, 2010.

[86] J. Biesner, L Schnieder, G Ahlers, Xiaoxiang Xie, KH Welge, MNR Ashfold, and RN Dixon. State selective photodissociation dynamics of a state ammonia. ii. *The Journal of Chemical Physics*, 91:2901, 1989.

[87] David H Mordaunt, Michael NR Ashfold, and Richard N Dixon. Photodissociation dynamics of ã state ammonia molecules. i. state dependent μ-v correlations in the nh2 (nd2) products. *The Journal of chemical physics*, 104(17): 6460–6471, 1996.

[88] Matthew L Costen and Gregory E Hall. Coherent and incoherent orientation and alignment of icn photoproducts. *Physical Chemistry Chemical Physics*, 9 (2):272–287, 2007.

[89] XF Yang, DW Hwang, JJ Lin, and X Ying. Dissociation dynamics of the water molecule on the a 1b1 electronic surface. *The Journal of Chemical Physics*, 113(23):10597–10604, 2000.

[90] Guang-Shuang-Mu Lin, Linsen Zhou, and Daiqian Xie. Theoretical study of the state-to-state photodissociation dynamics of the vibrationally excited water molecule in the b band. *The Journal of Physical Chemistry A*, 2014.

[91] K Weide and R Schinke. Photodissociation dynamics of water in the second absorption band. i. rotational state distributions of oh (2σ) and oh (2π). *The Journal of chemical physics*, 87(8):4627–4633, 1987.

[92] Wen Li, Steven D Chambreau, Sridhar A Lahankar, and Arthur G Suits. Megapixel ion imaging with standard video. *Review of scientific instruments*, 76(6):063106, 2005.

ABSTRACT

RYDBERG TIME-OF-FLIGHT AND IMAGING PROBES OF THE VELOCITY-DEPENDENT HYDROGEN ATOM SPIN POLARIZATION

by

BERNADETTE MICHLEWICZ BRODERICK

December 2014

Advisor: Dr. Arthur G. Suits

Major: Chemistry

Degree: Doctor of Philosophy

Insights into electron spin and nuclei are central to the field of chemical reaction dynamics. Of particular note is the study of spin-polarized hydrogen (SPH) atoms, which result from photodissociation of molecules. Examination of the de- tailed H-atom spin polarization is achieved by determining the projection of the electron spin onto the probe laser direction. In doing so, its angular distribution, complex dissociation pathways, and coherent excitation mechanisms may be revealed. Approaches to detect SPH atoms are experimentally challenging due to the difficulty associated with probing ground-state H atoms through isolated fine structure levels, which is the only direct way to achieve sensitivity to the ground- state m-distribution. Here, we present a novel methodology for direct detection of spin-polarized hydrogen atoms with high velocity resolution using variations of the Rydberg time-of-flight and ion imaging techniques. The approach described here utilizes three distinct geometries in addition to a unique double-resonance excitation scheme in order to fully characterize the H atom spin-polarization. In doing so, a general probe of multi-surface nonadiabatic dynamics is achieved, sensitive to

coherent effects in dissociation along multiple paths, and is applicable to a wide range of critical polyatomic systems.

AUTOBIOGRAPHICAL STATEMENT

Bernadette Broderick was born in 1986 in Detroit, MI. She received her Bachelor of Science in Chemistry from Saint Mary's College in Notre Dame, IN in 2008. She then worked in industrial Research and Development for 2 years before coming to Wayne State for graduate school in 2010.